ANNUAL REVIEWS

Annual Review of Earth and Planetary Sciences

The Composition of Earth's Lower Mantle

Motohiko Murakami,[1] Amir Khan,[1] Paolo A. Sossi,[1] Maxim D. Ballmer,[2] and Pinku Saha[1]

[1]Department of Earth Sciences, ETH Zürich, Zürich, Switzerland; email: motohiko.murakami@erdw.ethz.ch

[2]Department of Earth Sciences, University College London, London, United Kingdom

Annu. Rev. Earth Planet. Sci. 2024. 52:605–38

The *Annual Review of Earth and Planetary Sciences* is online at earth.annualreviews.org

https://doi.org/10.1146/annurev-earth-031621-075657

Keywords

lower mantle, chemical composition, Mg/Si ratio, mineralogy, seismic structure, density, thermal state, mantle convection, dynamical evolution

Abstract

Determining the composition of Earth's lower mantle, which constitutes almost half of its total volume, has been a central goal in the Earth sciences for more than a century given the constraints it places on Earth's origin and evolution. However, whether the major element chemistry of the lower mantle, in the form of, e.g., Mg/Si ratio, is similar to or different from the upper mantle remains debated. Here we use a multidisciplinary approach to address the question of the composition of Earth's lower mantle and, in turn, that of bulk silicate Earth (crust and mantle) by considering the evidence provided by geochemistry, geophysics, mineral physics, and geodynamics. Geochemical and geodynamical evidence largely agrees, indicating a lower-mantle molar Mg/Si of $\geq$1.12 ($\geq$1.15 for bulk silicate Earth), consistent with the rock record and accumulating evidence for whole-mantle stirring. However, mineral physics–informed profiles of seismic properties, based on a lower mantle made of bridgmanite and ferropericlase, point to Mg/Si $\sim$ 0.9–1.0 when compared with radial seismic reference models. This highlights the importance of considering the presence of additional minerals (e.g., calcium-perovskite and stishovite) and possibly suggests a lower mantle varying compositionally with depth. In closing, we discuss how we can improve our understanding of lower-mantle and bulk silicate Earth composition, including its impact on the light element budget of the core.

- The chemical composition of Earth's lower mantle is indispensable for understanding its origin and evolution.

- Earth's lower-mantle composition is reviewed from an integrated mineral physics, geophysical, geochemical, and geodynamical perspective.
- A lower-mantle molar Mg/Si of $\geq$1.12 is favored but not unique.
- New experiments investigating compositional effects of bridgmanite and ferropericlase elasticity are needed to further our insight.

1. INTRODUCTION

Earth's mantle is a mineralogical assemblage composed of silicates, principally containing MgO and SiO_2, that make up 80–85% of the mass of the bulk silicate Earth (BSE) (mantle and crust) (McDonough & Sun 1995, Palme & O'Neill 2014). It follows that the ratio of these oxides, expressed here as the molar Mg/Si ratio, controls the mineralogy of the mantle. In the upper mantle, high Mg/Si stabilizes olivine $(Mg,Fe)_2SiO_4$ at the expense of orthopyroxene $(Mg,Fe)SiO_3$, while ferropericlase (Mg,Fe)O replaces bridgmanite $(Mg,Fe)SiO_3$ in the lower mantle. Owing to its solid solution with Mg in silicate minerals, the quantity of iron—and indeed its valence state (occurring as Fe^0, Fe^{2+}, and Fe^{3+})—influences the stability of mantle phases. Therefore, despite its role in establishing mantle mineralogy and, in turn, physical properties (e.g., density, seismic velocities, viscosity), the composition of the BSE remains poorly constrained, particularly in the lower mantle.

This lack of information stems from the absence of direct samples, meaning geophysical techniques are an important constraint on lower-mantle structure and composition (e.g., Khan 2016). While seismology, because of its higher resolving power relative to other geophysical methods, has provided the most detailed information, electromagnetic sounding, gravity, and geodetic measurements yield complementary information related to the physico-chemical state of the mantle (e.g., Koyama et al. 2014; Lau et al. 2016, 2017). Moreover, direct measurements or first-principles simulations of the physical properties of relevant minerals and synthetic analogues at the conditions of the deep Earth allow for comparison with geophysical models that are constrained by field measurements (e.g., da Silva et al. 2000, Murakami et al. 2012). These sources constitute a large complement of information that aids in delineating possible compositions, thermal states, and hence mineralogies of Earth's lower mantle (Bina & Helffrich 2014).

Intimately related to the question of Earth's lower-mantle composition is that of the building blocks from which Earth accreted. Chondrites are thought to approximate the bulk composition of Earth, on the basis of the similarity of the proportions of their major constituents—Mg, Fe, Si, Ca, and Al—to those in Earth's accessible mantle (Ringwood 1966). Yet, this chondritic paradigm is strictly valid only for refractory elements, such as Ca and Al, whose relative abundances among chondrite groups are constant to within ~5%, whereas those of more volatile elements, such as Fe, Si, and Mg, vary markedly (Wasson & Kallemeyn 1988). Indeed, models for the composition of the BSE based on peridotites, rocks representative of the upper mantle, are found to have higher Mg/Si than among the chondritic meteorites (e.g., Hart & Zindler 1986, McDonough & Sun 1995, Workman & Hart 2005, Lyubetskaya & Korenaga 2007, Palme & O'Neill 2014). This difference could be the result of the accretion of Earth from nonchondritic components (e.g., O'Neill & Palme 2008), the accumulation of Si relative to Mg in the lower mantle, and/or the incorporation of Si into the core (Poirier 1994, Allègre et al. 1995). Determining the composition of the lower mantle thus helps to bracket the light element budget of the core, providing further constraints on the accretion, differentiation, and early evolution of our planet.

Should the lower mantle have a chemical composition distinct to that of the upper mantle, then dynamical mechanisms must have conspired over Earth's history to engender stratification.

Homogeneity in mantle composition on a global scale is often invoked, given that Earth's average upper-mantle composition (Ringwood 1975, Workman & Hart 2005) is able to satisfy a large range of geochemical and geophysical observations, including the mean radial mantle seismic velocity structure (e.g., Weidner 1985, Jackson & Rigden 1998), the average depth of the major mantle seismic discontinuities (e.g., Irifune 1994), and the mantle electrical conductivity structure (e.g., Xu et al. 2000, Grayver et al. 2017). Yet, despite these indications of a well-mixed mantle, there is ample seismic evidence to show that the mantle structure is more complex in detail, reflecting changes in temperature, chemical composition (Cammarano et al. 2005, Khan et al. 2009, Schuberth et al. 2009), and lithology, approximated as either mechanical mixtures (MMs) of basaltic and harzburgitic rocks or an equilibrium assemblage (EA) with different bulk compositions (Munch et al. 2020; Waszek et al. 2021; Bissig et al. 2022a,b; Tauzin et al. 2022). Moreover, geodynamical simulations indicate that Earth's mantle may operate in a hybrid regime between layered- and whole-mantle convection, e.g., with intermittent penetration of slabs into the lower mantle (e.g., Tackley et al. 2005). Indeed, lateral variations in rock viscosity and density associated with heterogeneity in Mg/Si (e.g., Xu et al. 2008, 2017; Tsujino et al. 2022) can delay mantle mixing and lead to segregation of distinct material (Manga 1996, Nakagawa & Buffett 2005, Ballmer et al. 2017a, Yan et al. 2020).

In this review, we examine existing geochemical and geophysical data to assess the degree to which the chemical composition of the lower mantle differs, if at all, from that of the upper mantle. To properly frame the problem, the compositions of samples from the upper mantle are compared with a chondritic BSE (Section 2). Deviations from the expected chondritic baseline may be accommodated, in part, by chemical differences between the upper and lower mantle. To determine whether this is the case, and in the absence of lower-mantle samples, we turn to geophysics and seismology to provide a new model of the velocity and density structure of the (lower) mantle (Section 3). We contrast these observations with measurements of the physical properties of thermodynamically stable mineral assemblages to constrain the composition and thermal state of the lower mantle (Section 4). Then geodynamic mechanisms are explored that can lead to chemical variability in the convecting mantle over time, within the bounds permitted by geochemical and geophysical observations (Section 5). Although these complementary approaches do not converge to a unique lower-mantle composition, they attest to abundances of the major elements in the upper and lower mantle lying within ~10% of each other and preclude drastic mineralogical changes at the whole-mantle scale.

2. GEO- AND COSMOCHEMICAL CONSTRAINTS ON EARTH'S LOWER-MANTLE COMPOSITION

2.1. Composition of the Upper Mantle

Modern models for the composition of the BSE exploit the chemical variability in global mantle peridotites to extrapolate to an assumed chondritic Ca/Al ratio (e.g., McDonough & Sun 1995, Palme & O'Neill 2014). This assumption is based on the fact that Ca and Al are both lithophile (i.e., near-absent in Earth's core) and cosmochemically refractory [i.e., condensing at temperatures higher than those of the major components, Mg, Si, and Fe—~1,350 K—from a solar composition gas at 10^{-4} bar (Lodders 2003)]. The Ca/Al ratio of chondrites varies by ~2.5% relative [excluding EL (low iron enstatite chondrites) (Wasson & Kallemeyn 1988)], such that chondritic ratios among refractory lithophile elements (RLEs) are expected to hold for Earth. By corollary, there is no requirement for the ratios of the major elements, Fe, Mg, and Si, to be chondritic in Earth. Indeed, the Fe/Mg ratio among chondrites varies by ~40% relative (Wasson & Kallemeyn 1988), rendering the concept of a chondritic composition for these elements a misnomer.

Consequently, the composition of the BSE, particularly for Fe, Mg, and Si, is best derived by other means.

Mantle peridotites from a variety of tectonic settings [e.g., xenolith and massifs (Canil 2004)] have rather constant SiO_2 contents, at 45.4 ± 0.3 wt%, as a function of their Mg#, Mg/[Mg + Fe^{2+}]. The Mg# is a proxy for mantle differentiation, either by partial melt extraction/addition (e.g., Herzberg 2004) or by mixing of mineralogical heterogeneities (e.g., Spray 1989, O'Neill & Palme 1998). Regardless of the mechanism, the constancy of SiO_2 in peridotites permits estimates of mantle Mg/Si, provided that the MgO abundance is known. The observations that the Mg#s of peridotites rarely extend below 0.89 and their FeO contents are uniform (8.1 ± 0.1 wt%) imply an MgO content of ∼36.8 wt%. This translates into an Mg/Si ratio of 1.21 ± 0.05, exceeding those of all known chondrites [0.73–1.07 (Wasson & Kallemeyn 1988)]; indeed, the superchondritic nature of Earth's upper mantle is well established (cf. Jagoutz et al. 1979, Ringwood 1979). Whether these chemical characteristics apply to the entire mantle is uncertain, as the sampled peridotites are all derived from the mantle lithosphere. Although some record geobarometric pressures up to ∼7–8 GPa (e.g., Boyd 1989), the majority are spinel lherzolites with equilibration pressures of ∼1–2 GPa [30–60 km (Walter 2003)], casting doubt over whether these samples are representative of Earth's convective mantle.

Inversion of the composition of mid-ocean ridge basalt (MORB) to calculate that of its source mantle can yield complementary estimates to peridotites. Because much of the upper mantle undergoes melting at mid-ocean ridges over time [∼10%/100 Myr by volume (Matthews et al. 2016)], the products (basaltic crust and harzburgitic residue) are, together, thought to be representative of the composition of the upper mantle (Ringwood 1979). The inferred MORB-source composition, termed pyrolite [or depleted MORB mantle (DMM)] (Workman & Hart 2005), is compositionally akin to sampled peridotites. However, the convecting upper mantle is not necessarily a good proxy for the BSE because there is no mandate for it to have chondritic RLE ratios. Indeed, the composition of the convecting upper mantle may be complementary to other, potentially unsampled reservoirs within the mantle (see Section 5). In any case, the Mg/Si of pyrolite/DMM is even more superchondritic [∼1.27 (Ringwood 1979, Workman & Hart 2005)] than that of the BSE as estimated from peridotites, assuming a chondritic Ca/Al ratio [∼1.21 (Palme & O'Neill 2014)]. The following, not mutually exclusive, possibilities for the superchondritic Mg/Si of Earth's upper mantle are (*a*) nonchondritic Mg/Si of Earth's building blocks, inherited from its accretion; (*b*) sequestration of some fraction of the Si into the core; and (*c*) chemical differences between the Mg/Si ratio of Earth's upper and lower mantles. Arguments for each of the three scenarios, the first two of which do not require a difference in the bulk compositions of the upper and lower mantle, are examined in more detail below.

2.2. Chemical and Isotopic Fractionation During Earth's Accretion

Cosmochemically, Earth falls at the end of a correlation between Fe/Si and Fe/Mg in chondrites (Yoshizaki & McDonough 2021, Khan et al. 2022) (**Figure 1**). However, there is no a priori reason to expect that Earth should lie on this line, owing to its nonchondritic nature in a number of element and isotope ratios [e.g., ^{142}Nd (Frossard et al. 2022)]. Nevertheless, it is reasonable to expect that Earth's composition lies on an extension of the chemical fractionation trends defined by chondrites, even if there is no one body that bears this composition. Such chemical variation could arise during condensation of the solar nebula (cf. Larimer 1967), where the Mg/Si ratio of chondrites depends on the relative proportions of olivine (Mg_2SiO_4) and orthopyroxene ($MgSiO_3$), with enstatite chondrites (ECs) having accumulated relatively more of the latter, resulting in their low Mg/Si ratios [∼0.73 (Wasson & Kallemeyn 1988)]. Their key condensation reactions are

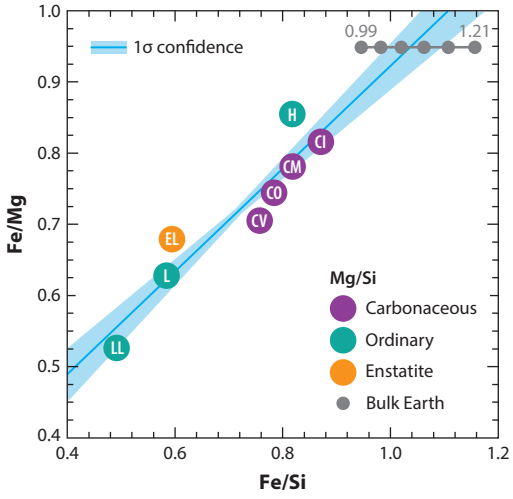

Figure 1

Distribution of molar Fe/Mg and Fe/Si within chondritic meteorites and for the bulk Earth for varying Mg/Si ratios from bulk silicate Earth–like at 1.21, as inferred from upper-mantle peridotites (Palme & O'Neill 2014), to 0.99, corresponding to a lower-mantle Mg/Si of 0.9 (i.e., entirely bridgmanitic), or a core Si content of 10 wt%. Ordinary chondrites are classified as those with high and low iron as Fe^0 (H and L, respectively) and low total iron (LL); carbonaceous (C) chondrites are grouped according to the type locality: Ivuna (CI), Murchison (CM), Ornans (CO), and Vigarano (CV); and enstatite (E) chondrites are classified relative to their high (EH) and low (EL) iron contents. The blue field represents the 1σ uncertainty on the regression. Data are from Wasson & Kallemeyn (1988).

given by

$$2\mathrm{Mg(g)} + \mathrm{SiO(g)} + 3/2\mathrm{O_2(g)} = \mathrm{Mg_2SiO_4(s)}, \quad 1.$$

$$\mathrm{Mg(g)} + \mathrm{SiO(g)} + \mathrm{O_2(g)} = \mathrm{MgSiO_3(s)}, \quad 2.$$

where g and s refer to gas and solid phase, respectively.

For a solar composition, Equation 1 proceeds to the right at higher temperatures (~1,380 K at 10^{-4} bar) than does Equation 2 (~1,300 K at 10^{-4} bar), resulting in an increase in the partial pressures (p), $p\mathrm{SiO}/p\mathrm{Mg}$, of the residual gas sufficient to promote condensation of $MgSiO_3$ (e.g., Yoneda & Grossman 1995). It follows that a simple model to explain the superchondritic Mg/Si ratio of Earth (should it reflect that of the BSE) would be that it accreted material that had preferentially accumulated olivine relative to orthopyroxene (e.g., the chemical complement to ECs).

Support for this scenario comes from Si isotopes (expressed as δ^{30}Si; the $^{30}Si/^{28}Si$ deviation from that of the NBS-28 standard), in which the BSE and Moon have δ^{30}Si that is distinctly heavier (-0.29 ± 0.03‰) than any chondrite. Chondrites span a range from about −0.7‰ (EH) [E chondrites are classified relative to their high (EH) and low (EL) iron contents] to about −0.4‰ for carbonaceous chondrites (Fitoussi et al. 2009). The δ^{30}Si is positively correlated with the Mg/Si ratio of the chondrite parent body or planet [including Earth, although heavily weighted by the ECs (Fitoussi et al. 2009)], while the δ^{26}Mg isotope ratio remains constant over the same Mg/Si interval (Dauphas et al. 2015). These observations can be understood in terms of equilibrium isotope fractionation between olivine and orthopyroxene and Mg- and Si-bearing gas species [reactions 1, 2 (Dauphas et al. 2015)]. The corresponding isotopic fractionation factor is $\Delta^{30}\mathrm{Si_{ol-gas}} = \delta^{30}\mathrm{Si_{ol}} - \delta^{30}\mathrm{Si_{gas}} \simeq 4 \times 10^6/T^2$, where T is temperature, while much of the Mg is

condensed into forsterite (compared to only 50% of the Si) by 1,300 K, meaning Mg isotopes remain essentially unfractionated from the nebular gas. Subtraction of an isotopically heavy, olivine-rich component would therefore simultaneously explain the chondritic δ^{26}Mg and the heavy δ^{30}Si composition of the BSE (Dauphas et al. 2015).

2.3. Evidence for Si in the Core

If Earth lies on the nebular trend (Dauphas et al. 2015) (**Figure 1**), then the inferred fraction of Si in the core (assuming a whole-mantle composition with Mg/Si = 1.21) is given by the intersection of the Mg/Si of the bulk Earth with that of the chondrite trend. However, the uncertainty on the trend is such that a wide range of Mg/Si ratios in the bulk Earth are permissible; **Figure 1** indicates a best-fit value of Mg/Si = 1.10 ± 0.06 and hence ∼4.5 ± 2.5 wt% Si in the core, indistinguishable from the $3.6^{+6.0}_{-3.6}$ wt% determined by Dauphas et al. (2015). A similar exercise was undertaken by O'Neill & Palme (1998) on the basis of Mg/Si versus Al/Si ratios, indicating that Earth would intersect the CC (carbonaceous chondrite) trend (which has constant Mg/Si = 1.06) with 5 wt% Si in the core. If correct, then this would suggest that, chemically, the material that accreted to form Earth had affinities to CCs (Witt-Eickschen et al. 2009, Sossi et al. 2018).

Independent indications for the siderophile behavior of Si come from metal-silicate partitioning and the light element content of the core that satisfies its geophysical properties, in particular the ∼10% density deficit relative to Fe-Ni alloy at the same *P-T* (Badro et al. 2014, Hirose et al. 2021), although we may note that the outer-core models of Irving et al. (2018) and Kemper (2023) (see also Section 3) are denser than the preliminary reference Earth model (PREM), (Dziewonski & Anderson 1981), which would act to reduce the aforementioned density deficit.

Silicon enters the core via the equilibrium,

$$SiO_2(l) + 2Fe(l) = Si(l) + 2FeO(l), \quad 3.$$

where l refers to liquid phase, implying that incorporation of Si into the core oxidizes Fe into FeO. Equation 3 proceeds to the right with increasing temperature and has only a weak dependence on pressure, as shown by free-energy and experimental data (O'Neill et al. 1998, Ricolleau et al. 2011). The corollary is that, because condensation of Si and Fe in the solar nebula took place at low temperatures (∼1,400 K at 10^{-4} bar), all Si condenses as olivine and orthopyroxene (Equations 1 and 2) and hence would have initially been present in Earth as an SiO_2 component. Insofar as this assumption is reasonable, Equation 3 implies that, for the 8.1 wt% FeO in Earth's mantle (in a closed system), 3.5 wt% Si is required in its core. This value coincides with that needed for the bulk Earth to intersect the carbonaceous chondrite trend in Mg/Si-Si isotope space (Dauphas et al. 2015) (see also **Figure 1**) and falls within the range predicted by heterogeneous accretion simulations of Earth (Ricolleau et al. 2011). Geophysical arguments also favor less than 4.5 wt% Si in the core on the basis of elastic properties of binary Fe-X mixtures (Badro et al. 2014, Umemoto & Hirose 2020) determined via ab initio calculations and their fit to the PREM, particularly to the density and V_P of the core (for a recent summary, see Hirose et al. 2021). This number may need revision, however, in light of new models of Earth's seismic profile [e.g., self-consistent Earth model (SCEM)] (Kemper 2023) (see Section 3) or the properties of metals at high pressures and temperatures.

2.4. Geochemical Constraints on Differences in Composition Between the Upper and Lower Mantle

Comparisons of the geochemical properties of a hypothetical BSE in the framework of a chondritic model for terrestrial accretion provide indirect constraints on the nature of the lower mantle.

Direct geochemical information may be obtained by probing the products of mantle melting, particularly those thought to have derived, at least partially, from the lower mantle.

2.4.1. SiO_2 exsolution from the core. While present-day seismic and geochemical constraints appear to favor ~4 wt% Si in the core (bulk Earth Mg/Si ~ 1.11), the initial budget of Si in the core may have been markedly higher, owing to its secular cooling. Because the equilibrium constant of Equation 3 increases with increasing temperature, cooling would have led to the exsolution of SiO_2 (Hirose et al. 2017, Helffrich et al. 2018; although see Huang et al. 2019). This excess SiO_2, hypothetically, could be stored in the lower mantle should subsequent convection fail to have chemically homogenized the mantle (see also Section 5). On contact with the lower mantle, it would react with ferropericlase to produce additional bridgmanite:

$$SiO_2(s,l) + (Mg,Fe)O(s) = (Mg,Fe)SiO_3(s). \quad 4.$$

The amount of SiO_2 exsolved cannot be uniquely constrained, as the initial conditions under which the core initially formed are unknown. Qualitatively, SiO_2 formation would require reduction of FeO initially in the mantle to Fe (Equation 3), which implies the core would have had to have formed under more oxidized conditions (i.e., higher FeO in the mantle) than observed today. As such, the process is self-limiting because higher FeO hinders Si dissolution into core-forming metal. Alternatively, SiO_2 may enter the lower mantle mechanically as stishovite (i.e., without reacting with ferropericlase according to Equation 4) due to convective instability of an SiO_2-enriched layer atop the core-mantle boundary (CMB) (Helffrich et al. 2018). Small stishovitic regions may float into the (lower) mantle, consistent with the detection of strong seismic scatterers (Kaneshima & Helffrich 2010). Partial melting products of the convecting mantle through time provide an independent record of the compositional differences, if any, between the lower and upper mantle.

2.4.2. The message from igneous rocks. The major element compositions of igneous rocks reflect those of their mantle sources. Because partial melts of peridotite are saturated in both olivine and orthopyroxene at low pressures (~0–4 GPa), their silica activities ($a SiO_2$) are buffered by the reaction

$$Mg_2SiO_4(s) + SiO_2(l) = 2MgSiO_3(s). \quad 5.$$

Owing to the partial molar volume change (ΔV) of Equation 5, liquids become poorer in silica (i.e., lower $a SiO_2$) as pressure increases. The SiO_2 contents of primitive MORB glasses [SiO_2 ~ 49 wt% (Jenner & O'Neill 2012)] are consistent with their derivation from 10–15% partial melting of an upper mantle with ~45 wt% SiO_2 and ~37 wt% MgO_2 [i.e., Mg/Si ~ 1.22 (Baker & Stolper 1994)].

At higher pressures (above 4 GPa), near-solidus partial melts of peridotite are no longer saturated in orthopyroxene (Walter 1998), meaning Equation 5 does not buffer $a SiO_2$. Experiments show that SiO_2 contents of partial melts of pyrolitic mantle (Mg/Si ~ 1.24) have a narrow range: 46–47.5 wt% for $3 < P\,(\text{GPa}) < 7$ at high melt fractions, $25 < F(\%) < 45$ (Walter 1998) (**Figure 2**). Although modern plume-derived magmas may be sourced, in part, from the lower mantle, they form by ~5–15% melting (Herzberg & Asimow 2015), over which SiO_2 varies significantly with F (**Figure 2**). This, together with their heterogeneous sources, renders them unsuitable for determining the mean composition of the convecting lower mantle. Komatiites are more amenable to this task, as they formed by higher degrees (~25–45%) of partial melting of near-primitive mantle (e.g., Nisbet et al. 1993, Sossi et al. 2016).

Most komatiite primary melts have between 45.5 and 49 wt% SiO_2 (Sossi et al. 2016), whereas the Commondale lavas (Wilson 2019) have ~50 wt% SiO_2 and contain primary orthopyroxene,

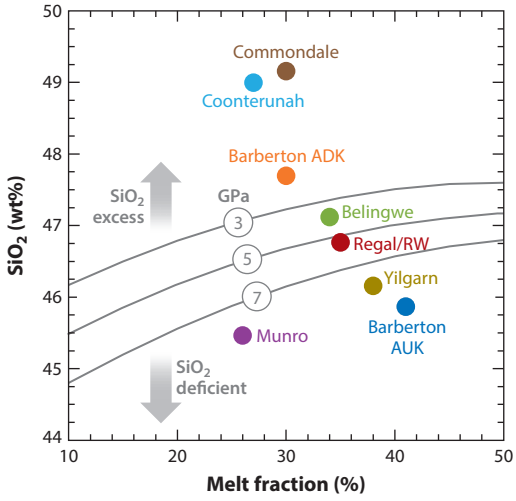

Figure 2

SiO_2 contents of komatiite parental melts (Sossi et al. 2016, Wilson 2019) as a function of their melt fraction, overlaid by curves of silicate liquids produced in partial melting experiments of West Kettle River peridotite (Mg/Si = 1.24) at different pressures: 3, 5, and 7 GPa [*circles* (Walter 1998)]. The majority of komatiite liquids are in equilibrium with their sources between ~3 and 7 GPa (cf. Sossi et al. 2016), and hence their compositions should lie within uncertainty (1–2% relative) of these curves. Departures therefrom may indicate silica deficiency or excess in their mantle sources, which are, in turn, relatively insensitive to uncertainties in melt fraction. Abbreviations: ADK, aluminum-depleted komatiite; AUK, aluminum-undepleted komatiite; RW, Ruth Well.

suggesting silica enrichment at the locus of melt extraction. Assuming a first-order linear relationship between the SiO_2 contents of silicate liquids and mantle Mg/Si, this permits a maximum Si enrichment over the BSE value of 5~10%. If representative of the lower mantle, it would imply an $(Mg/Si)_{LM} \sim 1.12$. Considering that the lower mantle comprises ~70% of the total mantle mass, the corresponding $(Mg/Si)_{BSE}$ would be ~1.15.

A complementary view on mantle composition is proffered by RLEs. Most komatiite suites have initial $^{176}Lu/^{177}Hf$ and $^{147}Sm/^{144}Nd$ compositions that lie on a line between the chondritic uniform reservoir (0.034 and 0.192, respectively) and DMM (0.039 and 0.216, respectively) (Puchtel et al. 2022, and references therein). That komatiite source regions can be reproduced by mixing between a DMM-like source residing in the upper mantle on the one hand and a chondritic reservoir on the other implies that there are no large-scale differences in the compositions of the (convecting) upper and lower mantle (see Section 5.3), at least with respect to RLEs. Some komatiites from the Kaapvaal craton diverge from this array, a feature suggested to reflect variable bridgmanite/ferropericlase ratios in their sources (Puchtel et al. 2022).

Walter et al. (2004) proposed that the marginally superchondritic Ca/Al ratio of the accessible mantle could arise from an ~10–20% enrichment of bridgmanite in the lower mantle (see also Jackson et al. 2014). However, as bridgmanite favors Hf ($D_{br/melt} = 2$) over Lu ($D_{br/melt} = 0.2$) (Walter et al. 2004, Liebske et al. 2005), this would produce subchondritic $^{176}Lu/^{177}Hf$ in hypothetical lower-mantle sources, which are not observed in any komatiites. Because the exchange coefficient $K_{D,br/melt}^{Mg/Si}$ approaches unity as $(Mg/Si)_{liquid=BSE}$ tends to 1, Si enrichment by bridgmanite accumulation becomes ineffective for hypothetical chondritic BSE compositions, and the observed value of $(Mg/Si)_{DMM} \sim 1.25$ cannot be achieved (Liebske et al. 2005). Indeed, 13% removal of a 96:4 br:ca-pv assemblage (the maximum permitted to retain chondritic Ca/Sc and Ca/Yb within

±10%) would only increase the Mg/Si ratio of the residual upper mantle by ∼2.5% (Liebske et al. 2005).

Chemical arguments suggest minimal preferential br/ca-pv accumulation in the lower mantle relative to the upper mantle, so as to maintain near-chondritic RLE ratios and Hf-Nd isotope compositions in ultramafic rocks. Nevertheless, these constraints are based on experiments near ∼25 GPa, whereas element partitioning at higher pressures may differ. The observed SiO_2 contents of komatiites are also consistent with upper mantle–like Mg/Si ratios (within 10% relative), placing limits on the Mg/Si ratio of the lower mantle to ≥1.12.

3. LOWER-MANTLE COMPOSITION AND THERMAL STATE: A GEOPHYSICAL PERSPECTIVE

Seismological constraints on Earth's mantle composition typically derive from a comparison of radial seismic models such as the PREM (Dziewonski & Anderson 1981) with laboratory measurements of the elastic properties of the relevant minerals at the appropriate pressures and temperatures (e.g., Ita & Stixrude 1992, Jackson 1998, Ganguly et al. 2009, Murakami et al. 2012). Because of the inherent limitations in qualitative comparisons, however, recent studies have sought to infer compositional and thermal parameters directly from seismic models and/or data based on geophysical properties that are computed using parameterized phase diagram approaches (e.g., da Silva et al. 2000, Trampert et al. 2004, Cammarano et al. 2005) or thermodynamically self-consistent methods (e.g., Bina 1998, Ricard et al. 2005, Khan et al. 2006, Matas et al. 2007, Cobden et al. 2009, Afonso et al. 2013, Fullea et al. 2021, Kemper 2023). The latter methods, which oftentimes rely on Gibbs free-energy minimization (Gfrem), allow for the prediction of seismic properties as a function of pressure, temperature, and bulk composition from thermodynamic data, as a consequence of the availability of comprehensive thermodynamic databases (e.g., Fabrichnaya et al. 2004; Stixrude & Lithgow-Bertelloni 2005, 2011, 2021; Khan et al. 2006; Piazzoni et al. 2007).

Several strategies exist for computing seismic properties from thermodynamic data, some of which rely on precomputed phase diagrams corresponding to fixed compositions and geotherms that are augmented with an external database of physical properties as implemented in, e.g., the Subduction Factory (Hacker & Abers 2004, Abers & Hacker 2016) and BurnMan (Myhill et al. 2023). Alternatively, Gfrem methods allow for computing seismic properties dynamically (i.e., on the fly) as a function of composition, temperature, and pressure as implemented in, e.g., Perple_X (Connolly 2009), HeFesto (Stixrude & Lithgow-Bertelloni 2011), MMA-EoS (Chust et al. 2017), and Phemgp (Zunino et al. 2011).

The immediate advantage of this approach is that size and location of discontinuities in seismic properties associated with pressure-induced mineralogical phase changes are modeled in a physically realistic manner, as their variations depend on composition, pressure, and temperature as illustrated in **Figure 3** for three mantle-relevant compositions. Another virtue of Gfrem over parameterized approaches is its versatility within an inverse framework, wherein thermochemical parameters are constrained directly from geophysical data (e.g., Khan 2016).

3.1. Mineralogical Predictions

The class of models with a homogeneous mantle whose composition is typified by varying Mg/Si ratios, as illustrated in **Figure 3**, reveals key first-order trends in the expected mineralogy of the lower mantle along an isentrope. Relative to the upper mantle, its phase assemblage is relatively simple; it comprises predominantly bridgmanite (general formula ABO_3 in the perovskite structure) and ferropericlase (typically $Mg_{1-x}Fe_xO$ in the rock-salt B1 structure), with the

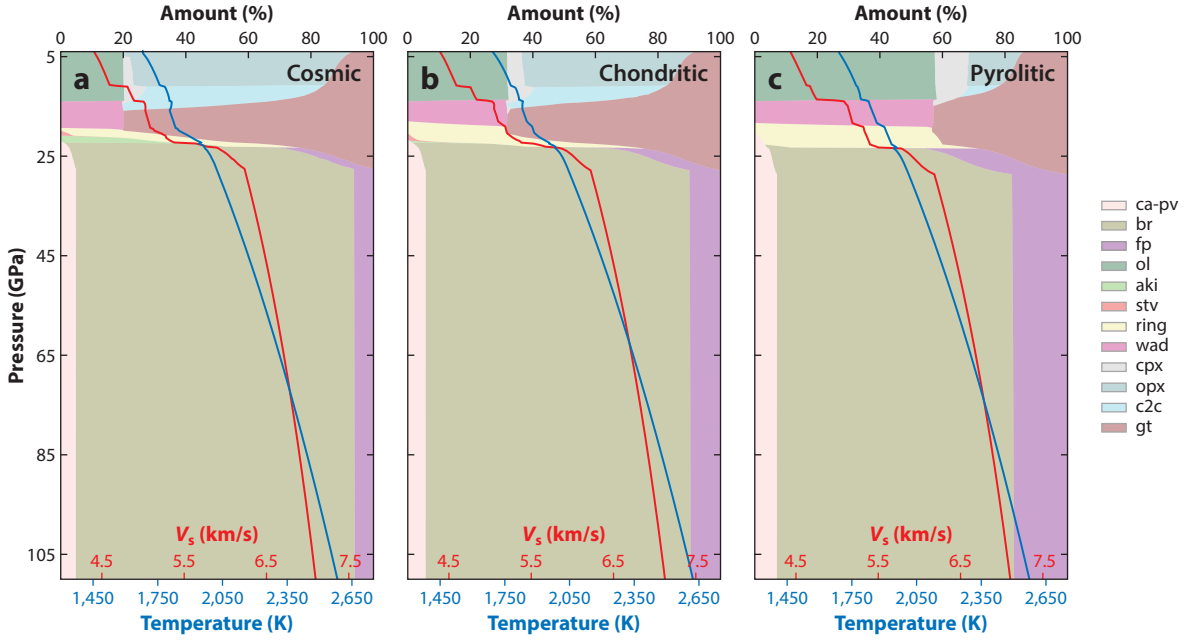

Figure 3

Illustration of variations in phase proportions, isotropic seismic shear-wave speed (V_S), and mantle isentropes (computed for a temperature of 1,648 K at 80 km depth) in the pressure range 5–110 GPa for three different hypothetical mantle compositions based on the equilibrium model: (*a*) cosmic (Mg/Si ~ 1), (*b*) chondritic (Mg/Si ~ 1.1), and (*c*) pyrolite (Mg/Si ~ 1.27) in the model chemical system comprising the oxides of the elements CaO-FeO-MgO-Al_2O_3-SiO_2-Na_2O. The phases are olivine (ol), orthopyroxene (opx), clinopyroxene (cpx), stishovite (stv), high-pressure Mg-rich cpx (c2c), garnet (gt), wadsleyite (wad), ringwoodite (ring), akimotoite (aki), calcium-perovskite (ca-pv), ferropericlase (fp), and bridgmanite (br). The seismic discontinuities are ol ⟶ wad (410), wad ⟶ ring (520), and ring ⟶ br + fp (660).

br/[fp + br] ratio being a negative function of Mg/Si. For a pyrolitic Mg/Si (=1.27), br/[fp + br] ~ 0.8, whereas for a cosmic Mg/Si of 1, it increases to ~0.95.

This dependence results from the near-absence of SiO_2 in ferropericlase [~1 wt% (Frost & Myhill 2016)], which is otherwise dominated by MgO and FeO, making bridgmanite the overwhelming host of Si in the lower mantle. Bridgmanite is predominantly composed of $MgSiO_3$, with ~10 mol% $FeSiO_3$, $FeAlO_3$, and $AlAlO_3$ components (Frost & Myhill 2016). Calcium-perovskite, whose modal abundance (~5 wt%) is constrained by the content of Ca, an RLE, of the lower mantle, has a composition close to end-member $CaSiO_3$. The ionic radius of Ca makes calcium-perovskite the prevailing host of large-ion lithophile elements, as well as rare-earth elements, U and Th, in the lower mantle (Corgne et al. 2005).

Consequently, the major elemental exchange reaction occurring in the lower mantle is among Mg and Fe^{2+} between bridgmanite and ferropericlase, given by

$$\mathrm{FeO(fp) + MgSiO_3(br) = MgO(fp) + FeSiO_3(br)}, \qquad 6.$$

and, at equilibrium,

$$K_D^{\mathrm{Fe-Mg}} = \frac{X^{\mathrm{br}}_{\mathrm{FeSiO_3}} X^{\mathrm{fp}}_{\mathrm{MgO}}}{X^{\mathrm{br}}_{\mathrm{MgSiO_3}} X^{\mathrm{fp}}_{\mathrm{FeO}}}, \qquad 7.$$

where X pertains to the mole fraction. In Equation 6, all Fe is presumed to be ferrous, and experimental data in Al-free systems indicate a near-constant K_D of ~0.2 between 25 and ~70 GPa,

before decreasing to ~0.05 by 100 GPa (Piet et al. 2016), likely owing to the high-spin (HS) to low-spin (LS) transition of Fe^{2+} in ferropericlase (Badro 2014). In Al-bearing systems, the substitution $FeAlO_3$ (where ferric iron resides on the dodecahedral A site) is energetically favored, resulting in an increase in the apparent K_D to ~0.5–0.8 (Frost & Myhill 2016, Piet et al. 2016, Huang et al. 2021). Therefore, at a given pressure and temperature, the elastic properties of bridgmanite and ferropericlase depend not only on X_{FeO} but also on its distribution between the two phases, the Fe^{3+}/Fe^{2+} in bridgmanite, and the extent of the spin transformation in ferrous iron in both ferropericlase and bridgmanite.

3.2. Methods for Geophysical Inversion of Lower-Mantle Composition

The interpretation of seismological models for Earth's lower mantle in terms of chemical composition and temperature is sensitive both to the details of the methodology employed and to uncertainties in key thermoelastic parameters of lower-mantle minerals. As a consequence, interpretations of the composition and thermal state of Earth's lower mantle have varied widely. More specifically, these discrepancies arise from a number of inconsistencies, including (*a*) the choice of mineral elastic parameters and the method by which these are extrapolated to lower-mantle conditions; (*b*) the choice of chemical system; (*c*) the consideration of bulk sound velocities only; (*d*) the nature of the geophysical data or model(s) against which the thermochemical models are compared, particularly in view of the fact that radial seismic reference models lack uncertainties; (*e*) incomplete consideration of uncertainties associated with thermoelastic parameters of relevant minerals; and (*f*) the nature of the conversion from thermochemical to seismic parameters. Moreover, arguments have been advanced supporting the case for mantle material consisting of an MM rather than an EA of minerals on the grounds that the former provides a better fit to the seismic wave speeds of radial reference models in the transition zone structure (Xu et al. 2008). However, the arguments put forward by Xu et al. (2008) in favor of MM over EA are purely qualitative (see also discussion in Bina & Helffrich 2014). Quantitative analysis, meanwhile, indicates (e.g., Munch et al. 2020, Bissig et al. 2022a) that regional- and global-scale seismic waveform data are matched to a similar extent by either parameterization, although chemical equilibration appears to be less prevalent underneath stable cratonic regions, yet neither of them are capable of completely matching the seismic wave velocity gradients in the mantle transition zone (Bissig et al. 2022b).

Exemplary of the class of studies that rely on a model of physical properties supplemented with an account of phase equilibria based on a graphical summary of experimental data is that by Cammarano et al. (2005). Mantle mineralogy is fixed on the basis of a pyrolitic composition and a specified geotherm. Physical properties in the form of bulk and shear moduli, their pressure and temperature derivatives, and thermal expansion vary separately within specified bounds. Because of the restrictions imposed by the parameterization, their ability to fit the geophysical data (global P- and S-wave travel times) is severely limited, leading to the suggestion that other compositions in the lower mantle, possibly in combination with a superadiabatic thermal gradient, are needed.

Representative of studies that rely on thermodynamic self-consistency is that of Matas et al. (2007). While composition and geotherm are varied (the former also with depth), and, in turn, mineralogy and bulk seismic properties, inversion is restricted to fitting a radial seismic velocity profile (AK135) with unspecified uncertainties. The importance of this study lies in the incorporation of model parameter uncertainties in the inversion that impact the elastic properties of the major lower-mantle minerals.

In addition to considering the uncertainties associated with the elastic parameters, Cobden et al. (2009) also explored the influence of the assumed equation-of-state (EoS) in modeling lower-mantle composition and temperature. Based on matching radial reference profiles, Cobden et al. (2009) found that a superadiabatic temperature gradient in combination with a lower-mantle

composition that becomes increasingly enriched in a basaltic component with depth provides the best results but also concluded that a lower mantle consisting of adiabatic pyrolite cannot be ruled out completely.

A more comprehensive approach is to combine the different pieces, i.e., data and results from mineral physics experiments, geochemical and petrological analyses of mantle minerals, and geophysical inverse calculations, to directly transform geophysical data into the mantle composition and thermal state. This approach is illustrated by, e.g., Khan et al. (2006) and Khan et al. (2008), who inverted long-period electromagnetic sounding data and global seismic travel-time data for Earth's mantle composition and thermal state, respectively. The results generally agreed with earlier geophysically derived conductivity and seismic velocity models and indicated most probable CMB temperatures of around 3,200 K and bulk Earth Mg/Si ratios of 1.05–1.15, intermediate between a cosmic and a chondritric composition.

Common to these studies, however, are limitations in assessing the uncertainties in computed geophysical properties. Parameterized phase diagram approaches, for example, are only able to consider the uncertainty in the elastic properties of the minerals and ignore the uncertainty associated with the identity and the compositions of the stable minerals, thereby underestimating the overall uncertainty. Generally, uncertainties of 0.5–1%, 1–2%, and 2–4% in mantle density, P-wave speed, and S-wave speed, respectively, are found (Kuskov & Fabrichnaya 1994, Connolly & Kerrick 2002, Kennett & Jackson 2009, Connolly & Khan 2016). The thermodynamic model precludes consideration of redox effects that may be important if native or ferric iron are present in the lower mantle. Finally, the thermodynamic model also precludes consideration of minor phases and components such as water and melt due to lack of thermodynamic data, although these are not expected to be important in the lower mantle with the exception of maybe D'', which is beyond the scope of this review.

Table 1 summarizes a selection of studies in terms of estimates of lower-mantle composition and thermal state and other modeling details. To further constrain the wide compositional range, integration of seismic modeling with experimental mineral physics measurements of relevant materials at the pressure and temperature conditions of the lower mantle is required.

4. EXPERIMENTAL MINERAL PHYSICS: CONSTRAINTS FROM ELASTICITY

4.1. Experimental Considerations

A first-order means toward constraining the mineralogy and, in turn, the chemistry of the lower mantle is to directly compare seismic reference models with mineral properties determined experimentally under relevant high-pressure and high-temperature conditions (Section 3). Significant technical progress over the past few decades in in situ high-pressure sound velocity measurements using Brillouin light scattering (BLS) combined with a diamond anvil cell (DAC) has enabled the determination of longitudinal sound and transverse wave speeds (hereinafter V_P and V_S) of mantle phases under lower-mantle pressures (~25–135 GPa). Earth's lower mantle largely consists of two minerals, bridgmanite and ferropericlase (Irifune et al. 2010), and, depending on composition, minor amounts (~7 vol%) of calcium-perovskite (see **Figure 3**). Thus, V_P and V_S profiles of the lower mantle can, to a first approximation, be constructed from V_P and V_S measurements of these two minerals. This extends earlier inferences that were based on extrapolation of measurements obtained at low pressure (for a review, see Murakami 2013). Here, we review the status of high-pressure V_P and V_S measurements of bridgmanite and ferropericlase with a special emphasis on V_S velocities, which were primarily obtained by BLS within the lower-mantle pressure range, and discuss mineralogical models of the lower mantle.

Table 1 Summary of geophysical estimates of LM composition and thermal state

Study	Temperature at top of LM	Temperature at core-mantle boundary	LM thermal gradient	LM Mg/Si (mol)	Observational constraints	Comparison	Mineralogical model/ compositional dependence	Chemical system
Jackson 1998	1,850 K	2,300 K	Adiabatic	1.27	A	Forward model	Parameterized phase diagram/no	FMS
Marton & Cohen 2002	1,800 K	2,400 K	Adiabatic	1.27	A	Forward model (ab initio)	Parameterized phase diagram/no	CFMAS
da Silva et al. 2000	1,900 K	4,000 K	Superadiabatic	1.27	A	Forward model (ab initio)	Parameterized phase diagram/no	CFMAS
Trampert et al. 2004	NA	3,750 K	Superadiabatic	1.27	A	Random sampling	Parameterized phase diagram/yes	FMS
Cammarano et al. 2005	1,873 K	2,400 K	Adiabatic	1.27	B	Random sampling	Parameterized phase diagram/no	NA
Mattern et al. 2005	1,800 K 2,200 K 2,500 K	2,000 K 2,500 K 2,700 K	Subadiabatic Subadiabatic Subadiabatic	1.27 1.07 1.03	A	Inversion	Thermodynamic/yes	CFMAS
Khan et al. 2006	1,900 K	3,200 K	Superadiabatic	1.09	C	Inversion	Thermodynamic/yes	CFMAS
Matas et al. 2007	1,935 K[a] 1,926 K[a] 1,875 K[a]	2,972 K 2,942 K 2,702 K	Superadiabatic Superadiabatic Superadiabatic	1.03 1.07 1.27	A	Inversion	Thermodynamic/yes	CFMAS
Khan et al. 2008	1,700 K	2,700 K	Superadiabatic	1.35	D	Inversion	Thermodynamic/yes	CFMAS
Cobden et al. 2009	1,900 K	3,100 K[b]	Superadiabatic	1.0–1.4	A	Inversion	Thermodynamic/yes	CFMAS
Kemper 2023	1,900 K	2,600 K	Isentropes	≥1.4	E	Inversion	Thermodynamic/yes	NCFMAS

Only mean values are indicated, but uncertainties of temperature and Mg/Si, where no ranges are given, are at least ±10%. For more details, the reader is referred to the original studies.
A = radial seismic reference model; B = International Seismological Centre global mantle P- and S-wave travel times, fundamental spheroidal and toroidal normal modes, and mass; C = global electromagnetic induction data and mean mass and moment of inertia; D = ISC global mantle P- and S-wave travel times and mean mass and moment of inertia; E = normal modes, mantle, and core body wave travel times, mean mass and moment of inertia, and tidal response. The model chemical systems used in the various studies include FMS, CFMAS, and NCFMAS, comprising the oxides FeO-MgO-SiO_2, CaO-FeO-MgO-Al_2O_3-SiO_2, and NaO_2-CaO-FeO-MgO-Al_2O_3-SiO_2, respectively. Abbreviations: LM, lower mantle; NA, not available.
[a]Temperature at 810 km depth.
[b]Temperature at 2,500 km depth.

The BLS technique is based on the inelastic light scattering related to the photon-phonon interaction between the probe laser and thermally generated phonon in a sample. The V_P and V_S of a sample in a DAC placed in symmetric platelet geometry are obtained from the shift in frequency ($\Delta\omega$) according to

$$V_i = \frac{\Delta\omega_i \lambda}{2\sin(\theta/2)}, \quad 8.$$

where λ is the laser wavelength, θ is the external scattering angle, and i denotes either shear or longitudinal mode. Because the BLS technique in a DAC is based on the scattered light transmitted through a sample, as long as the sample is sufficiently transparent, a combination of the BLS technique and DAC serves as an effective method to determine V_P and V_S in situ under extremely high-pressure conditions (Murakami et al. 2009).

With this method, V_P and V_S data of materials making up Earth's interior have been extensively collected from single-crystal samples since the 1970s (e.g., Weidner et al. 1975). However, due to technical issues (for more discussion, see, e.g., Murakami 2013), most of the results from single-crystal measurements were limited to relatively low pressures (~30–40 GPa), which are insufficient to constrain the mineralogy of the entire lower mantle. For example, Kurnosov et al. (2017) report the sound velocity of single-crystal Fe- and Al-bearing bridgmanite up to ~40 GPa, which was found to be compatible with a pyrolitic (Mg/Si ≈ 1.27) uppermost lower mantle consisting of bridgmanite ~80 vol% based on comparison with the PREM. However, extrapolating their velocity profile to higher pressures results in large deviations from the PREM at depths below 1,200 km, indicative of significant uncertainties with this procedure (Lin et al. 2018). Recent experimental efforts by Criniti et al. (2021) and Fu et al. (2023) on single-crystal V_P and V_S measurements of lower-mantle phases have extended pressures to ~80 GPa. Criniti et al. (2021) reported V_P and V_S measurements of pure $MgSiO_3$ bridgmanite to 79 GPa by carefully aligning the orientation of the diamond anvils to observe both V_P and V_S of bridgmanite using the BLS technique. Their studies also support a model of the lower mantle made up of pyrolite (to mid- to lower-mantle depths). Comparison of Criniti et al. (2021) and Kurnosov et al. (2017) indicates that 10 mol% of the $FeAlO_3$ component (in which Fe is ferric) in bridgmanite results in a decrease of K_{S0}, G_0, and K', while increasing G', where the former two are the bulk adiabatic and shear modulus at zero pressure and the latter two refer to bulk adiabatic and shear modulus pressure derivative. This result is counter to recent measurements on single-crystal $Mg_{0.88}Fe_{0.1}Al_{0.14}Si_{0.90}O_3$ bridgmanite by Fu et al. (2023) that were performed up to 82 GPa using BLS in combination with an impulsive stimulated light scattering method. Fu et al. (2023) showed that the incorporation of Al and Fe in bridgmanite reduces G_0 and increases G', while the effect on K_{S0} and K' appears to be insignificant. The results of Fu et al. (2023) are compatible with a bridgmanite-enriched lower mantle consisting of up to 89 vol% br.

The first V_S data of bridgmanite determined under lower-mantle pressure conditions were obtained at pressures up to 96 GPa using polycrystalline $MgSiO_3$ bridgmanite synthesized in situ at the pressure-temperature conditions of the lower mantle in a laser-heated DAC. This result allows for a significant extension of the pressure limit of BLS measurements (Murakami et al. 2007b). Since then, V_P and V_S of polycrystalline silicate samples have successfully been measured to pressures of ~170 GPa (Murakami et al. 2007b). With this newly developed high-pressure BLS method, all subsequent V_S measurements of polycrystalline br, including Al- and Fe-bearing bridgmanite (Murakami et al. 2012, Mashino et al. 2020), were carried out at pressures equivalent to those covering the lower mantle. The measured transverse elastic properties (shear modulus and its pressure derivative) of both bridgmanite and ferropericlase at lower-mantle pressures are summarized in **Figure 4**.

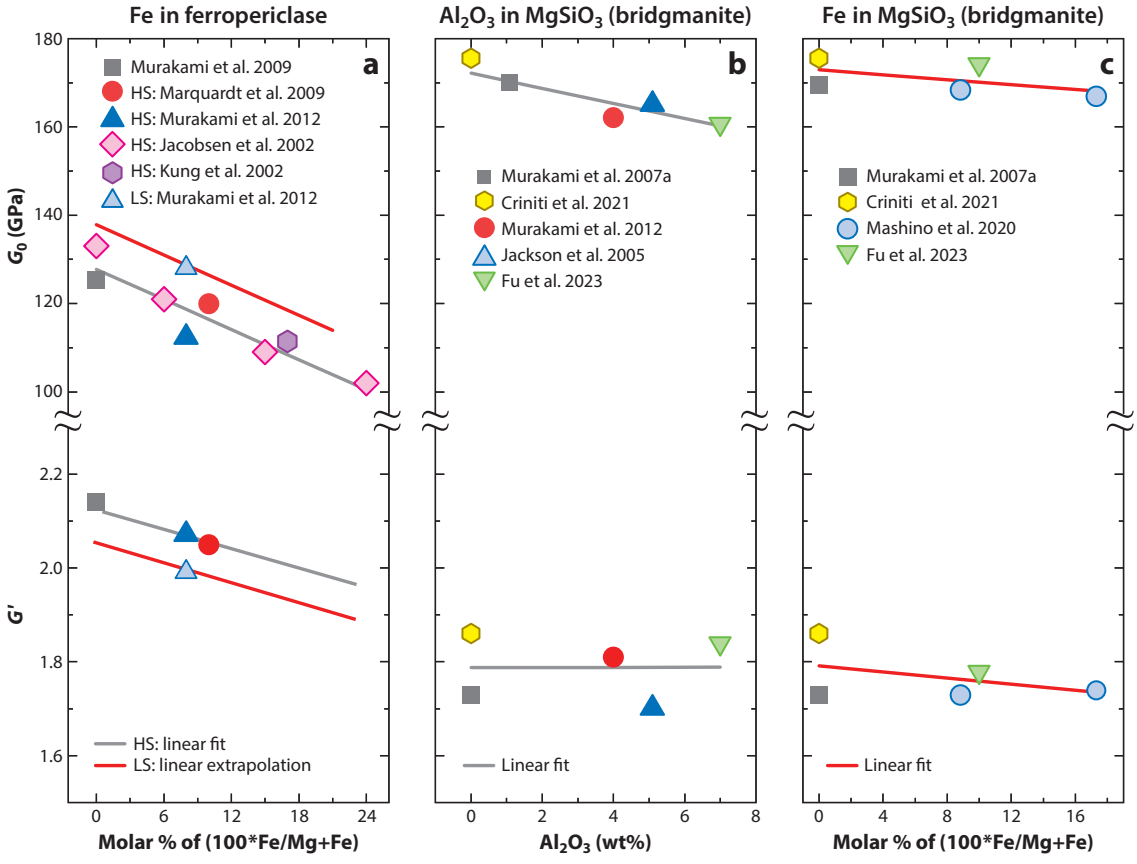

Figure 4

Summary of recent experimental mineral physics measurements of shear modulus (G_0) and its pressure derivative (G') as a function of composition: variation of G_0 and G' with respect to Fe in ferropericlase (fp) (*a*), Al_2O_3 in $MgSiO_3$ [bridgmanite (br)] (*b*), and Fe in $MgSiO_3$ (br) (*c*). Solid gray and red lines represent the fitted linear dependence of G_0 and G' with pressure. Note that the low-spin (LS) state (*red line*) assumes the same linear dependence as the high-spin (HS) state of fp.

4.2. Constructing Lower-Mantle Seismic Profiles from Experimental Data

The longitudinal sound and transverse elastic properties of both bridgmanite and ferropericlase obtained at lower-mantle pressures using the BLS method are summarized in **Table 2**. Here, we focus on a lower-mantle mineralogical model constructed by combining all the data. In the modeling procedure, shear modulus (G_0) and its pressure derivative (G') play an essential role, where G' is obtained from fitting high-pressure shear modulus (G) as a function of finite strain (ϵ). Moreover, to extract the consistent elastic properties of the lower-mantle phases over the entire lower-mantle pressure range, it is important that all data are fitted using a single formalism. Accordingly, we employ the third-order Eulerian finite-strain equation (Stixrude & Lithgow-Bertelloni 2005) to refit the existing polycrystalline data, given that improper truncation of the finite-strain equation could result in up to ~10% difference in estimated G' values (e.g., Fu et al. 2023, Myhill et al. 2023):

$$G = (1+2\epsilon)^{\frac{5}{2}} G_0 + (3K_{S0}G' - 5G_0)\epsilon + (12K_{S0}G' - 48K_{S0} - 28G_0 + 9K_{S0}K')\epsilon^2 \qquad 9.$$

Table 2 Thermoelastic properties of lower-mantle phases

Formula phase	Reference	P (GPa)	V_0 (cm^3/mol)	G_0 (GPa)	G'	K_{T0} (GPa)	K'_T	K_{S0} (GPa)	K'	θ_0 (K)	γ_0	η_{S0}	q
Polycrystalline study													
MgO, periclase	Murakami et al. 2009	14–129	11.24	125.2	2.14	NA	NA	163[a]	3.8[a]	NA	NA	NA	NA
$Mg_{0.92}Fe_{0.08}O$ HS, ferropericlase	Murakami et al. 2012	0–120	11.32	112.2	2.07	152[b]	4[b]	NA	NA	NA	NA	NA	NA
$Mg_{0.92}Fe_{0.08}O$ LS, ferropericlase	Murakami et al. 2012	0–120	11.03	127.9	1.99	170[b]	4[b]	NA	NA	NA	NA	NA	NA
$MgSiO_3$, bridgmanite	Murakami et al. 2007a	8–96	24.43	169.6	1.73	NA	NA	257.1[c]	3.71[c]	NA	NA	NA	NA
$MgSiO_3$ + 4 wt% Al_2O_3, bridgmanite	Murakami et al. 2012	42–124	24.51	162.2	1.81	NA	NA	252[d]	3.7[d]	NA	NA	NA	NA
$Mg_{0.93}Fe^{2+}_{0.07}Fe^{3+}_{0.02}Si_{0.98}O_3$, bridgmanite	Mashino et al. 2020	26–105	24.54	168.4	1.73	256[e]	4[e]	NA	NA	NA	NA	NA	NA
$Mg_{0.86}Fe^{2+}_{0.15}Fe^{3+}_{0.03}Si_{0.97}O_3$, bridgmanite	Mashino et al. 2020	26–124	24.64	167	1.74	257[f]	4[f]	NA	NA	NA	NA	NA	NA
Single-crystal study													
$Mg_{0.9}Fe_{0.1}O$, ferropericlase	Marquardt et al. 2009	0–70	11.34	120	2.05	151	4.1	NA	NA	NA	NA	NA	NA
$MgSiO_3$, bridgmanite	Criniti et al. 2021	0–79	NA	175.6	1.86	NA	NA	257.1	3.71	NA	NA	NA	NA
$Mg_{0.88}Fe_{0.1}Al_{0.14}Si_{0.9}O_3$, bridgmanite	Fu et al. 2023	25–82	NA	211[g]	1.66[g]	NA	NA	326[g]	3.32[g]	NA	NA	NA	NA

(*Continued*)

Table 2 (*Continued*)

Formula phase	Reference	P (GPa)	V_0 (cm^3/mol)	G_0 (GPa)	G'	K_{T0} (GPa)	K'_T	K_{S0} (GPa)	K'	Θ_0 (K)	γ_0	η_{S0}	q
Two-phase aggregate modeling													
$Mg_{0.79}Fe_{0.21}O$ HS, ferropericlase	This study	NA	11.45[h]	104	1.88	158[b]	4[b]	NA	NA	686[h]	1.39[h]	2.2[h]	1.7[h]
$Mg_{0.79}Fe_{0.21}O$ LS, ferropericlase	This study	NA	11.17[h]	113	1.84	170[b]	4[b]	NA	NA	686[h]	1.39[h]	2.2[h]	1.7[h]
$X_{Fe} = 0.06 + 4$ wt% Al_2O_3, bridgmanite	This study	NA	24.50	164.4	1.77	NA	NA	251[j]	3.86[j]	905[i]	1.57[i]	2.6[i]	1.1[i]
$X_{Fe} = 0.1 + 4$ wt% Al_2O_3, bridgmanite	This study	NA	24.57	163.3	1.76	NA	NA	249[j]	3.90[j]	905[i]	1.57[i]	2.6[i]	1.1[i]

V_0 = ambient volume; G_0 & G' = shear modulus at ambient pressure and temperature and its pressure derivative; K_{T0} & K'_T = isothermal bulk modulus at ambient pressure and temperature and its pressure derivative; K_{S0} & K' = adiabatic bulk modulus at ambient pressure and temperature and its pressure derivative; Θ_0 = Debye temperature; γ_0 = Grüneisen parameter; η_{S0} = shear strain derivative of γ_0, $q = \frac{\partial \ln \gamma}{\partial \ln V}$. Abbreviations: HS, high spin; LS, low spin; NA, not applicable.

[a]Sinogeikin & Bass (2000).
[b]Fei et al. (2007).
[c]Criniti et al. (2021).
[d]Jackson et al. (2005).
[e]Dorfman & Duffy (2014).
[f]Lundin et al. (2008).
[g]Values at 25 GPa.
[h]Myhill et al. (2023).
[i]Stixrude & Lithgow-Bertelloni (2011).
[j]Fu et al. (2023).

with

$$\epsilon = \frac{1}{2}\left[\left(\frac{\rho}{\rho_0}\right)^{\frac{2}{3}} - 1\right], \quad 10.$$

where ρ_0 and ρ are the sample density at ambient conditions and at high pressure estimated from X-ray diffraction measurements, respectively, while G is obtained from the BLS measurements. Incidentally, the same formalism is employed in Section 3 above. The refitted G_0 and G' values are summarized in **Table 2**. The thermal pressure ($P_{\rm th}$) and temperature effect on G ($G_{\rm th}$) and K ($K_{\rm th}$) are incorporated through the Mie-Grüneisen-Debye EoS (Stixrude & Lithgow-Bertelloni 2005) using the following expressions:

$$P_{\rm th}(V,T) = \frac{\gamma_0 \Delta U}{V}, \quad K_{\rm th}(V,T) = (\gamma_0 + 1 - q)\frac{\gamma_0 \Delta U}{V} - \gamma_0^2 \frac{\Delta(C_{\rm V} T)}{V}, \quad \text{and} \quad G_{\rm th}(V,T) = \frac{-\eta_{\rm S0}}{V}, \quad 11.$$

where ΔU is the internal energy at room temperature, γ_0 is the Grüneisen parameter, $C_{\rm V}$ is the specific heat at constant volume, q is the logarithmic derivative of the Grüneisen parameter with respect to volume, $\eta_{\rm S0}$ is the shear-dependent part of the finite-strain generalization of the Grüneisen parameter, V is volume, and Δ refers to change in parameter(s). After evaluating thermoelastic parameters of each mineral at corresponding lower-mantle pressure and temperature, they are combined to estimate $V_{\rm P}$ and $V_{\rm S}$ of the multiphase assemblage using the Voigt-Reuss-Hill average.

The effect of Fe in ferropericlase on G_0 and G' in the HS and LS states and the effect of Fe and Al_2O_3 in bridgmanite (Badro 2014) on G_0 and G' are shown in **Figure 4**. Because there is only a single $V_{\rm P}$ and $V_{\rm S}$ measurement of ferropericlase (8 mol% Fe) in the LS state (Murakami et al. 2012), the effect of iron content on the elasticity of ferropericlase in the LS state is estimated assuming that the change in trend is similar to that in the HS state. The effect of the spin transition on the elasticity of bridgmanite is neglected as it remains unclear whether bridgmanite is affected at all (Badro 2014, Kurnosov et al. 2017, Mashino et al. 2020).

The resulting compositional effect on the shear modulus and its pressure derivative of bridgmanite is

$$G_0 = 172.92 - 1.71 \times Al_2O_3 - 27.83 \times \frac{\rm Fe}{\rm Fe + Mg} \quad 12.$$

$$G' = 1.79 + 8.169 \times 10^{-5} \times Al_2O_3 - 0.326 \times \frac{\rm Fe}{\rm Fe + Mg}, \quad 13.$$

while the compositional effect on the shear modulus and its pressure derivative of ferropericlase is given by

$$G_0 = 127.8_{\rm HS}/137_{\rm LS} - 113.83 \times \frac{\rm Fe}{\rm Fe + Mg} \quad 14.$$

$$G' = 2.13_{\rm HS}/2.08_{\rm LS} - 1.182 \times \frac{\rm Fe}{\rm Fe + Mg}, \quad 15.$$

where Al_2O_3 and Fe/(Fe + Mg) are given in terms of wt% and mole fraction, respectively, and G_0 in GPa. $V_{\rm P}$ and $V_{\rm S}$ are subsequently obtained from the usual expressions,

$$V_{\rm P} = \sqrt{\frac{K_{\rm S} + \frac{4}{3}G}{\rho}} \quad \text{and} \quad V_{\rm S} = \sqrt{\frac{G}{\rho}}, \quad 16.$$

where K_S and G are the adiabatic bulk and shear modulus at the desired lower-mantle pressure and temperature. For the dependence of K_S on Al_2O_3 and Fe/(Fe + Mg), we followed Fu et al. (2023).

4.3. Combining Mineral Physics and Geophysical Constraints

To constrain the lower-mantle mineral assemblage and, in turn, composition, we construct lower-mantle mineral physics V_P, V_S, and density profiles relying on the assumption that the lower mantle is principally made up of the major minerals bridgmanite and ferropericlase. We attempt to find the mineral physics models for a range of bridgmanite/ferropericlase ratios, corresponding to volume fractions of 70%:30%, 80%:20%, 90%:10%, and 100%:0% that provide the best fit to a radial seismic profile. For the present purposes of comparing lower-mantle seismic profiles based on the mineral physics data and EoSs compiled here, we rely on the lower-mantle geophysically constrained adiabats (isentropes) of Kemper (2023), which, as indicated in **Figure 5*a***, are similar (within measurement, observational, and modeling uncertainties) to the laboratory-based peridotite geotherm of Katsura (2022). At the basis of the SCEM of Kemper (2023) are mantle and outer core–sensitive body waves, and the most up-to-date astronomic-geodetic measurements of mean mass and mean normalized moment of inertia (MoI), including the degree-2 tidal response in the form of the Love numbers k_2 and h_2. We resort to using this model here because PREM

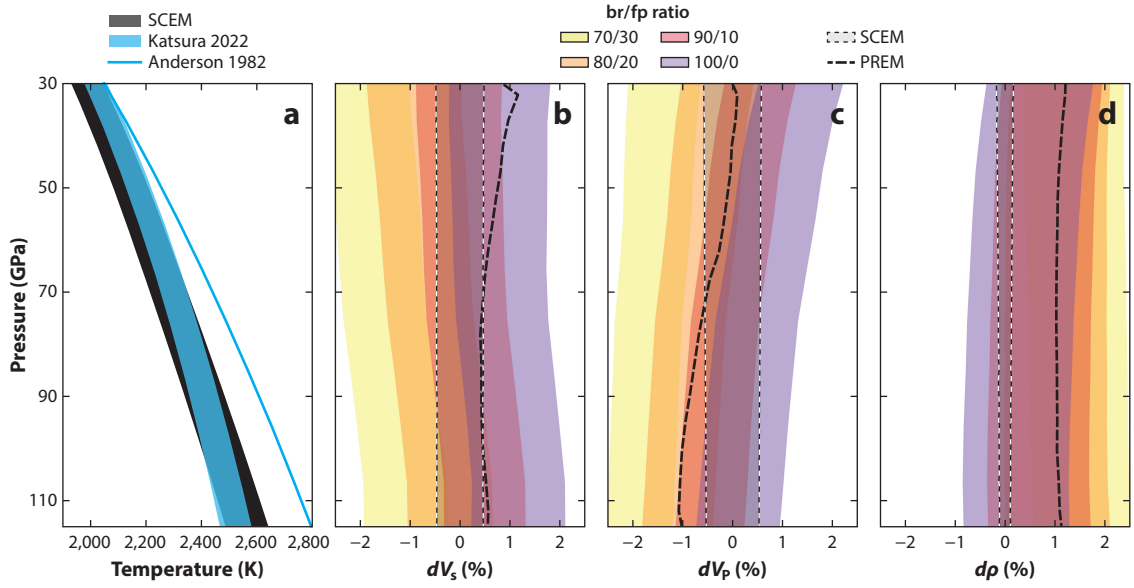

Figure 5

Comparison between experimentally constrained mineral physics (MP) and geophysically determined lower-mantle seismic wave speed profiles. (*a*) Representative lower-mantle geotherms: the laboratory-based peridotite adiabat of Katsura (2022), the geophysically constrained isentropes based on the self-consistent Earth models (SCEM) of Kemper (2023), and the superadiabat of Anderson (1982). (*b–d*) Lower-mantle MP and SCEM S-wave speed (V_S), P-wave speed (V_P), and density (ρ) profiles. Panels *b–d* indicate relative differences computed as $dX = (X_{MP} - \hat{X}_{SCEM})/\hat{X}_{SCEM}$, where X is either V_S, V_P, or ρ and $\hat{X}_{SCEM}$ and X_{MP} are the equivalent properties in MP and mean SCEM models, respectively. The MP models in panels *b–d* are based on Monte Carlo modeling to account for measurement uncertainties in composition and MP parameters and computed along the SCEM geotherms for a lower mantle made up of a representative range of bridgmanite/ferropericlase (br/fp) ratios (indicated by the numbers in the legend). The range in SCEM profiles shown here represents the 50% credible interval of the sampled model range. See the main text for details.

is incompatible with the recent measurements of MoI and k_2 and h_2, and only matches current normal-mode data qualitatively (Kemper 2023).

To account for additional uncertainties associated with the mineral physics– and composition-related parameters that enter into the EoS (Equations 12–15), we conduct a Monte Carlo search of all relevant parameters. For each of the mineral configurations, we randomly vary the Al_2O_3 content in the range 3.8–4 wt% and Fe in bridgmanite and ferropericlase between 6–10 mol% and 20–22 mol%, respectively, while temperature varies between the upper and lower bounds of SCEM shown in **Figure 5*a***. The partition coefficient, K_D, of Fe between bridgmanite and ferropericlase presently varies between 0.23 and 0.44, which is consistent with previous work (e.g., Murakami et al. 2005, Sinmyo et al. 2008, Irifune et al. 2010). The EoS parameters K_0, K', and V_0 are varied within ±0.5%, ±0.75%, and ±0.5%, respectively, relative to the values listed in **Table 2**. For the four constant-mineralogical models, this corresponds to variations in Mg/Si between 1.35–1.39 (bridgmanite/ferropericlase ∼ 70%:30%), 1.19–1.24 (bridgmanite/ferropericlase ∼ 80%:20%), 1.07–1.12 (bridgmanite/ferropericlase ∼ 90%:10%), and 1 (bridgmanite/ferropericlase ∼ 100%:0%), respectively. These parameter ranges provide a reasonable coverage of measurement uncertainties of various experimental groups (including Jackson & Rigden 1998, Murakami et al. 2012, Mashino et al. 2020, Fu et al. 2023). Aggregate V_P, V_S, and density profiles were computed using BurnMan (Myhill et al. 2023) and are shown in **Figure 5*b–d*** as relative differences to the mean SCEM.

From our analysis and **Figure 5**, we can draw several conclusions. First, the combined variations in temperature, composition, and mineral physics parameters correspond to changes in V_S, V_P, and density of ∼1.3%, ∼1%, and ∼1.2%, respectively. Similar variations are obtained when changing the bridgmanite/ferropericlase ratio by 10%. In comparison, uncertainties in V_S, V_P, and density in SCEM are ∼0.8%, ∼1.2%, and ∼0.2%, respectively. Second, constant-compositional models with Mg/Si ≥ 1.2 are generally too slow and too dense, while models with Mg/Si ≤ 1.2 fare better, particularly as Mg/Si approaches 1. Third, V_S can be matched by a constant-compositional lower mantle with an Mg/Si ∼ 1–1.12, corresponding to a bridgmanite volume fraction of 90–100%. In turn, the relative V_P profiles suggest a mineralogical, and therefore compositional, gradient with Mg/Si decreasing from ∼1.19–1.24 in the 30–50 GPa pressure range to 1.07–1.12 in the mid- to lower mantle (50–80 GPa) to 1–1.12 in the lowermost mantle (80–115 GPa), corresponding to an increasing bridgmanite fraction with depth. Finally, the mineral physics models presented in **Figure 5** yield higher densities than SCEM, except for the pure bridgmanite model (Mg/Si ∼ 1). Of our models, the latter model is also the only one capable of matching V_P, V_S, and density simultaneously across most of the lower mantle within uncertainty. Thus, we may summarize the comparison between geophysics and mineral physics as pointing to a cosmic lower-mantle composition with an Mg/Si close to 1.

In interpreting the mineral physics profiles, however, a number of issues come into play that are of relevance for the present comparison. The mineral physics models are based on a minimum parameterization that, while allowing for variations in lower mineralogy (through changes in bridgmanite/ferropericlase ratio), do not account for the thermally and compositionally driven changes in bridgmanite/ferropericlase ratio as a function of temperature, Al_2O_3, and Fe, nor is the effect of the latter on Mg/Si fully captured. Also, adiabatic thermal conditions are implicit in our calculations. Although models with larger degrees of freedom (e.g., sub- and superadiabatic conditions, increase in the number of components in chemical model) are permissible, these only act to increase nonuniqueness and were therefore not considered in the construction of SCEM.

To study the impact of a superadiabatic lower-mantle geothermal gradient, we considered the geotherm of Anderson (1982) (**Figure 5*a***) and re-performed the Monte Carlo sampling of the mineral physics profiles as described above. The comparison (not shown) based on the

thermal profile of Anderson (1982) indicates, as expected, a decrease in all modeled properties so as to produce changes in dV_S, dV_P, and $d\rho$ relative to the properties computed using SCEM of about −0.75%, −0.3%, and −0.2%, respectively, exacerbating the match to the pure bridgmanite model. Because a superadiabatic lower mantle consisting purely of bridgmanite is unlikely to be realistic, this could possibly be an indicator for subadiabatic lower-mantle conditions, consistent with geodynamic models (e.g., Yan et al. 2020). Finally, as illustrated in **Figure 3**, the mineral phase calcium-perovskite is stable throughout the lower mantle at levels of ∼5 vol%. To investigate the effect of calcium-perovskite on mineral physics profiles, we recomputed V_S, V_P, and density by allocating 5 vol% of bridgmanite/ferropericlase to calcium-perovskite. The resultant changes in dV_S, dV_P, and $d\rho$ are around 0.2%, −0.1%, and 0.3%, respectively, and therefore insignificant.

5. THE COMPOSITION OF EARTH'S LOWER MANTLE IN THE CONTEXT OF EARTH EVOLUTION AND DYNAMICS

Numerical models of long-term mantle convection can be used to integrate geochemical and geophysical data, placing them into the context of mantle structural evolution. However, the predictions of global-scale mantle-evolution models can strongly depend on the assumed initial condition, especially in terms of any compositional layering due to mantle differentiation (e.g., Davaille 1999, Kellogg et al. 1999). The initial thermochemical structure of the mantle is set in the aftermath of the Moon-forming giant impact, during which the entire mantle was likely molten as a global magma ocean (MO) (Nakajima & Stevenson 2015), but remains poorly understood.

5.1. Heterogeneity Formation in the Early Earth

Chemical fractionation during the crystallization of a deep MO governs the initial composition of the mantle, crust, and atmosphere. Initially, the hot MO cools quickly and convects vigorously. As first crystals form, they either settle gravitationally (fractional crystallization) or remain in suspension (batch crystallization). In the latter case, a mush that behaves similar to a solid is formed at ∼40% crystal fraction (Costa et al. 2009). The dominance of either mode of crystallization depends on the efficiency of crystal nucleation and growth, the liquid-solid density contrast, the viscosity of the silicate liquid, and the MO cooling history (Lebrun et al. 2013, Solomatov 2015). While fractional crystallization is likely dominant in the upper mantle (Solomatov 2015, Xie et al. 2020), the mode of lower-mantle MO crystallization remains poorly understood.

For any reasonable starting compositions of the whole-mantle MO [Mg/Si of 1.21∼1.25 (Ringwood 1979, McDonough & Sun 1995, Palme & O'Neill 2014) or possibly lower], Mg-rich bridgmanite is the first phase to crystallize from the lower-mantle MO (Boukaré et al. 2015, Caracas et al. 2019, Nabiei et al. 2021). For efficient crystal setting (i.e., fractional crystallization), this implies a silica-enriched initial composition of the lower mantle with Mg/Si close to 1. For end-member batch crystallization [also referred to as equilibrium crystallization (Solomatov 2015)], the lower mantle would, in turn, assume a BSE composition in the aftermath of MO crystallization. However, end-member batch crystallization without any melt-solid segregation remains highly unlikely. Indeed, the crystal mush that is formed during batch crystallization cools very slowly. On the relevant timescales [of solid-state convection (Solomatov 2015)], melt-solid segregation due to coupled melt percolation and solid compaction should be efficient, possibly aided by convection (Holtzman et al. 2003, Ballmer et al. 2017b, Hier-Majumder & Hirschmann 2017, Caracas et al. 2019). As soon as the melt is extracted from the mush, the remaining solid is again a cumulate pile of bridgmanite with similar compositions as for fractional crystallization (Caracas et al. 2019). Thus, both end-member modes of MO crystallization lead to significant

bridgmanite fractionation during Earth mantle differentiation and possibly a silica-enriched lower mantle.

Alternative scenarios for the sequestration of silica-enriched heterogeneity in the early Earth involve incomplete equilibration of the mantle in the aftermath of a Moon-forming giant impact (Deng et al. 2019), as well as exsolution of SiO_2 from the core (Hirose et al. 2017, Helffrich et al. 2018). Assuming that significant amounts of silica have been partitioned into the core at the high-temperature conditions of the Moon-forming impact (Hirose et al. 2017), the flux of SiO_2 from the core to the mantle is $\sim 8 \times 10^{21}$ kg per 100 K of core cooling (Helffrich et al. 2018). For CMB temperatures $\geq$4,750, the thermally coupled core-MO system is fully molten (Boukaré et al. 2015), such that any exsolved SiO_2 would be efficiently mixed across the BSE. For core temperatures of roughly 4,750$\sim$4,000 K, the mantle should be separated into two layers, i.e., a basal magma ocean (BMO) and the overlying MO/mantle (Labrosse et al. 2007, Boukaré et al. 2015, Caracas et al. 2019, Miyazaki & Korenaga 2019). Over this temperature range, the core can deliver up to $\sim 5.7 \times 10^{22}$ kg of SiO_2 (i.e., $\sim$2 wt% of the lower mantle's mass) to the BMO. After BMO freezing, the core continues to deliver SiO_2 to the lower mantle as small-scale blobs (Helffrich et al. 2018), but related amounts are small, as the BMO solidus (Boukaré et al. 2015, Miyazaki & Korenaga 2019) is close to the temperature of the present-day CMB (e.g., Anzellini et al. 2013, Nomura et al. 2014). Another process to deliver silica to the lowermost mantle is the overturn of Hadean crust (Tolstikhin & Hofmann 2005), but this material may again interact with the BMO.

The crystallization of such an SiO_2-enriched BMO would have similar consequences for the fractionation of bridgmanitic cumulates as discussed above for the whole-mantle MO. For silica-normative [i.e., roughly molar (Mg + Fe)/Si $\leq$ 1.0] starting compositions, evolved BMO cumulates may involve some stishovite (SiO_2) (Boukaré et al. 2015). The total amount of fractionated bridgmanitic/stishovitic cumulates depends on the initial volume of the BMO (Caracas et al. 2019), as well as the influx of (Hadean) crust from above and core-exsolved SiO_2 from below.

5.2. Heterogeneity Preservation During Long-Term Mantle Evolution

While it appears likely that silica-enriched materials are formed in the early Earth, it remains uncertain whether such primordial heterogeneity can be preserved over time in the solid-state convecting mantle. Seismic images of subducted slabs that sink through the mantle (e.g., Van Der Meer et al. 2010), as well as of mantle plumes that rise from the CMB to the base of the lithosphere (French & Romanowicz 2015), support the notion that the mantle convects as a whole. Whole-mantle convection is highly efficient in mixing the mantle, particularly in the plate-tectonic regime (Ferrachat & Ricard 1998, O'Neill & Zhang 2018). At face value, this would imply that the lower mantle has essentially the same bulk composition as the pyrolitic uppermost mantle and thus a relatively high Mg/Si ratio of $\sim$1.26. Considering lithospheric recycling over billions of years, most of the mantle is accordingly thought to be a small-scale MM of recycled slab components, consistent with seismic observations (Morgan & Morgan 1999, Xu et al. 2008, Waszek et al. 2021, Goes et al. 2022) (also see Section 3). A MM of $\sim$20% mafic/basaltic and $\sim$80% harzburgitic rocks (i.e., with a basalt fraction $f = 0.2$) approximates a pyrolitic composition with Mg/Si $\approx$ 1.27, consistent with MORB-source compositions (Ringwood 1975, 1979; Workman & Hart 2005; Xu et al. 2008) and volume estimates of past subduction (Morgan & Morgan 1999).

However, several geophysical observations are at odds with a mantle that is homogeneous on large scales with $f \approx 0.2$. For example, seismic profiles such as the PREM and SCEM cannot be matched with a uniform adiabatic mantle (for details, see Section 4.3). In addition, some subducted slabs stagnate at $\sim$1,000 km depth (Fukao & Obayashi 2013), which is difficult to reconcile with

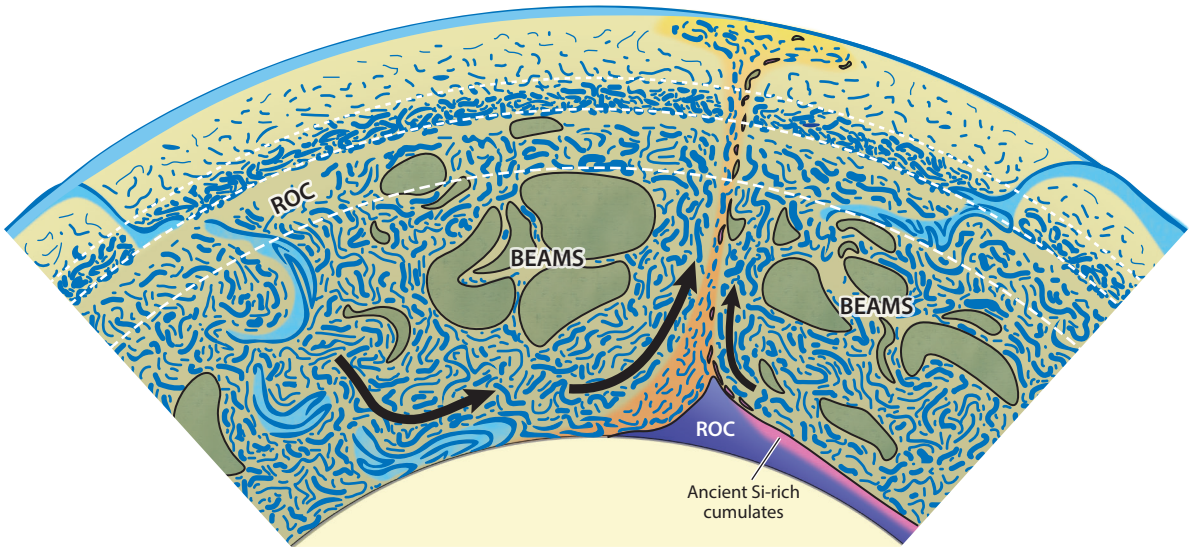

Figure 6

Visualization of a potential style of material preservation and present-day mantle structure, as based on geodynamic-model predictions. Recycled oceanic crust (ROC) is enriched in the transition zone and lower mantle. Bridgmanitic material may be preserved as bridgmanite-enriched ancient mantle structures (BEAMS) in the mid-mantle, e.g., explaining slab stagnation. Additional Si-enriched materials may be stored as piles in the lowermost mantle and sampled by plumes (*yellow*). The depicted mantle structure is silica enriched compared to a well-mixed mantle (e.g., mechanical mixture with $f = 20\%$) but remains consistent with whole-mantle convection and thus close to an end-member model in terms of silica enrichment (see Section 5.3). Dashed lines mark depths of 410, 660, and 1,000 km. Figure adapted from Gülcher et al. (2021).

a well-stirred mantle, as this depth range is far from phase transformations (**Figure 3**). While a viscosity jump, which is also inferred at ∼1,000 km depth from geoid inversion (Rudolph et al. 2015), may provide a viable explanation for slab stagnation, it does not readily account for the deflection of several plumes in a similar depth range (French & Romanowicz 2015), and more importantly, its occurrence by itself remains enigmatic. Intermediate-scale (thousands of kilometers across) seismic reflectors/refractors in the uppermost lower mantle indicate regional compositional anomalies, possibly enriched in silica (Jenkins et al. 2017, Waszek et al. 2018). Thus, it cannot be ruled out that primordial heterogeneity (e.g., MO cumulates) is preserved in the lower mantle (Ballmer et al. 2017a).

Modeling studies have demonstrated that significant preservation is indeed geodynamically feasible as long as the primordial material is intrinsically viscous (Ballmer et al. 2017a; Gülcher et al. 2020, 2021). In these models, primordial material, initially imposed as a thick basal layer, can be preserved as small blobs to large domains in the mid-lower mantle (**Figure 6**), as up- and downwellings tend to flow around them to minimize viscous dissipation. These domains have been referred to as bridgmanite-enriched ancient mantle structures (BEAMS). They are thought to host bridgmanitic MO cumulates, but any primordial material would be preserved in a similar way, as long as their physical properties agree with those modeled. Over 4∼5 billion years model time, preservation is most efficient (8∼30% of lower-mantle volume) for a viscosity of primordial material that is ≥2 orders of magnitude (and a density that is slightly) higher than the rest of the mantle. These physical properties are realistic for (slightly iron-enriched) bridgmanite (Tsujino et al. 2022), particularly when taking into consideration that the viscosity of ultramafic rocks should be controlled by that of ferropericlase (Girard et al. 2016), and that grain growth in

bridgmanitic rocks is highly efficient (Fei et al. 2023). They are also consistent with primordial compositions that involve SiO_2 stishovite, which is even more viscous than bridgmanite (Xu et al. 2017).

Assuming that primordial materials are purely bridgmanitic, the implications in terms of BSE Mg/Si can be estimated. The sequestration of bridgmanitic material with a mass of $X_{bm} \leq 13\%$ of that of the mantle is within the range of that predicted by geodynamic models for BEAMS and remains consistent with chondritic Ca/Sc and Ca/Yb (Liebske et al. 2005) (see also Section 2). Assuming that this material is buried in the lower mantle, and independent of its geometry (e.g., as BEAMS, small blobs, or otherwise), it would shift the BSE Mg/Si ratio from ~1.27 (i.e., convecting mantle with $f = 0.2$) (see above) to ≥1.22.

Even though BEAMS potentially provide an attractive reservoir for excess silica in the lower mantle, to date, there is no unequivocal evidence for their actual presence and long-term preservation. Models predict the roofs of BEAMS to be typically located at 800~1,200 km depth (Gülcher et al. 2020, 2021), consistent with the depths of regional seismic reflectors/refractors, the inferred viscosity jump, and stagnant slabs. However, the BEAMS model is difficult to test by seismic tomography, as bridgmanite is only slightly faster than a pyrolitic bridgmanite-ferropericlase assemblage (80/20 in **Figure 5**). Moreover, geodynamic models predict that BEAMS are also slightly warmer than the ambient mantle (Gülcher et al. 2021) and hence trade off with their slightly higher intrinsic thermoelastic properties. That being said, comparison of the footprints of relatively fast versus slow S- and P-velocity regions in the mid-lower mantle is consistent with BEAMS (Shephard et al. 2021). Additional studies are needed to further test the BEAMS hypothesis, particularly exploiting seismic attenuation and anisotropy, or even magnetotellurics, but at present, all these methods have a limited resolution in the lower mantle.

5.3. Enrichment of Basaltic Rocks in the Convecting Lower Mantle

In contrast to BEAMS, which evolve from an intrinsically strong layer of MO cumulates, an alternative scenario for silica sequestration in the lower mantle is independent of the initial condition of mantle convection. Significant amounts of basaltic rocks have been recycled into the mantle over billions of years (Morgan & Morgan 1999). Even before the onset of plate tectonics, crustal recycling has likely been efficient during alternative regimes of global tectonics (Sizova et al. 2010, Moore & Webb 2013, Lourenço et al. 2020). Basaltic rocks are denser than ultramafic rocks (e.g., pyrolite, harzburgite) across most of the mantle, except for a narrow depth range between 660 km and 700~750 km depth. Due to this density crossover, geodynamic models predict that the mantle transition zone acts as a basalt filter, such that small-scale basaltic heterogeneity tends to be enhanced in the transition zone as well as the lower mantle relative to the upper mantle (Nakagawa & Buffett 2005, Ballmer et al. 2015, Yan et al. 2020). These model predictions are well supported by seismic precursor studies, which provide evidence for a heterogeneous and basalt-enriched transition zone (Bissig et al. 2022b, Goes et al. 2022, Tauzin et al. 2022).

A picture emerges in which the convecting mantle is still an MM of mafic (ancient and modern recycled basalt) and ultramafic (harzburgite and peridotite/pyrolite) rocks, but with variable proportions (i.e., variable f) across the mantle. According to Yan et al. (2020), an average $f \approx 0.25$ in the convecting mantle corresponds to a pyrolitic uppermost mantle (i.e., $f \approx 0.2$), balanced by higher f in the transition zone and lower mantle. This model is overall consistent with seismic constraints for $f \approx 0.2$–0.5 in the transition zone (Munch et al. 2020; Bissig et al. 2022a,b; Tauzin et al. 2022) and implies Mg/Si ≈ 1.2 for the BSE, in accord with primitive-mantle estimates of Mg/Si ≈ 1.21 (see Section 2). A more precise estimate not just is limited by model limitations and choices in Yan et al. (2020) but moreover requires assumptions on how much of the basaltic

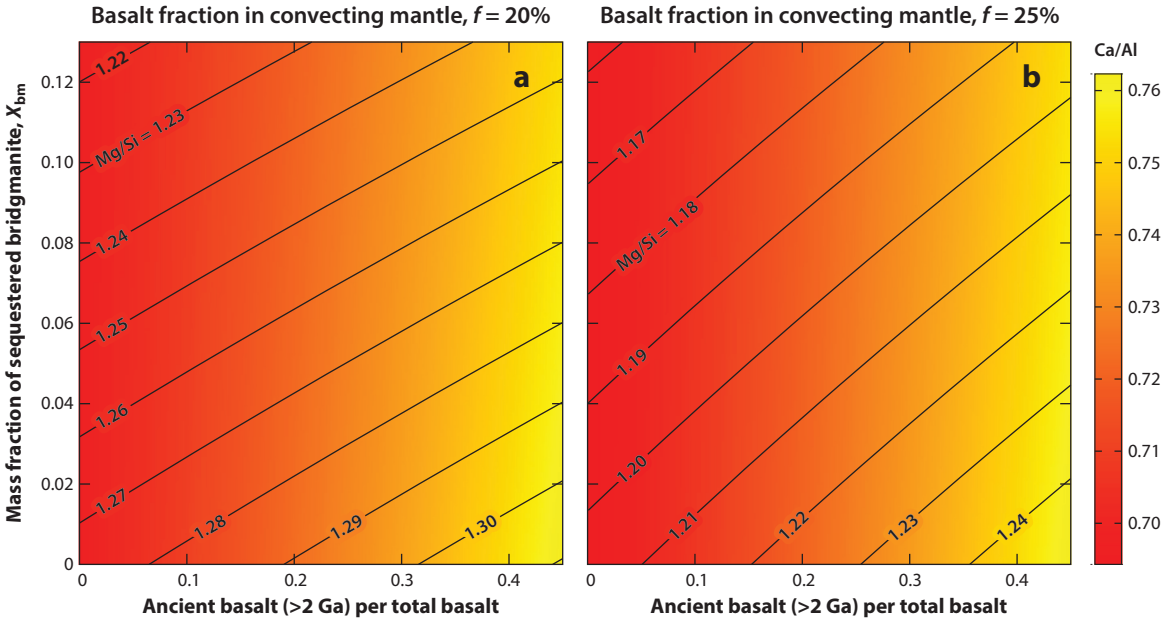

Figure 7

Bulk silicate Earth composition (*contours*: molar Mg/Si; *colors*: molar Ca/Al) for a mantle that consists of preserved bridgmanite with fractions of X_{bm} within a basalt-harzburgite mechanical mixture. In this mechanical mixture, basalt fractions are (*a*) $f = 20\%$ and (*b*) $f = 25\%$. The basaltic component within this mixture is partly modern mid-ocean ridge basalt (MORB) and partly ancient basalt with ages ≥2 Ga as labeled (*x* axis). Bridgmanite (magma-ocean cumulates), harzburgite, modern MORB, and ancient basalt compositions are from Caracas et al. (2019), Baker & Beckett (1999), Workman & Hart (2005), and Herzberg et al. (2010), respectively.

material that floats in the lower mantle [or is piled up at its base (Brandenburg & Van Keken 2007)] is modern MORB, and how much of it is ancient basaltic material. Ancient basalts with ages ≥2 Ga display significantly higher Mg/Si and Ca/Al than modern MORB (Herzberg et al. 2010) and thus tend to shift inferred BSE values as long as they are preserved in significant fractions. Indeed, significant preservation of ancient recycled crust in the lower mantle is consistent with geodynamic modeling (Yan et al. 2020) and isotope geochemical data (Cabral et al. 2013).

5.4. Implications for BSE Composition

Figure 7 summarizes the coupled effects of ancient basalt and bridgmanite preservation, as well as those of total basalt fraction (f) in the convecting mantle, on BSE Mg/Si and Ca/Al. Neglecting the basalt filter (i.e., $f \approx 0.2$), BSE Mg/Si are generally high, even for significant bridgmanite preservation. The minimum permitted Mg/Si is ~1.24 as long as significant fractions of basaltic material stored in the mantle are ancient (≥2 Ga), a condition to match chondritic Ca/Al of 0.72~0.74 (McDonough & Sun 1995, Palme & O'Neill 2014). Taking into account the basalt filter (i.e., $f \approx 0.25$), BSE Mg/Si can be significantly lower, i.e., well within the range of primitive-mantle compositions (Palme & O'Neill 2014). Combining the effects of the basalt filter with those of bridgmanite preservation ($X_{bm} \leq 0.13$, e.g., due to BEAMS) allows Mg/Si of the BSE of ~1.18 (or higher), and further neglecting ancient-basalt preservation, of ~1.16 (or higher). These BSE Mg/Si correspond to lower-mantle Mg/Si of 1.14~1.16.

It should be noted that these values are likely lower bounds. Lower-mantle bridgmanite preservation may be less efficient than assumed above, depending on the viscosity and density of the

bridgmanitic layer formed during Earth differentiation (Gülcher et al. 2020, 2021). However, exsolution of SiO_2 from the core (Hirose et al. 2017, Helffrich et al. 2018) can further reduce lower-mantle Mg/Si, but just by up to ~0.02. This limited effect is because exsolution primarily occurs during the lifetime of the BMO (see Section 5.1) and is thus already included in the budget of bridgmanitic cumulates above, unless BMO cumulates include significant fractions of stishovite (see Section 5.1) and are preserved in the lower mantle, a model that has testable geophysical implications (Yang & Wu 2014). Independent of their origin, the large low-velocity provinces are another potentially silica-enriched reservoir (Trampert et al. 2004, Vilella et al. 2021). However, as long as they are made up of basalt (or materials with similar Mg/Si), their effects are already included in the budget discussed above (**Figure 7**).

6. SUMMARY

If the mantle has been recycled and stirred efficiently due to plate subduction for at least 2–3 Gyrs (Korenaga 2013), a BSE Mg/Si ratio significantly lower than 1.15–1.18 seems unlikely based on geodynamical considerations (Section 5). However, there is still significant debate over changes in mantle convection patterns throughout Earth's history. The compilation of geochemical studies indicates a lower-mantle Mg/Si of 1.12–1.16. (Section 2.4). For a simplified bi-mineralic model, these Mg/Si values translate to a bridgmanite-to-ferropericlase volume ratio of ~85:15. The mineral physics approach, which involves comparing experimentally determined seismic wave velocity data with a radial seismic model, overall points to a cosmic lower-mantle composition with an Mg/Si ratio close to 1 (~100% bridgmanite). However, the assumed lower-mantle mineral assemblage of bridgmanite and ferropericlase may be too simplistic to account for the potential mismatch between the experimental data and seismic model. To comprehensively explain the apparent mismatch with seismic reference models, it may be necessary to consider radial variations in bulk composition and, notably, small- to medium-scale lateral heterogeneity. The mantle is heterogeneous on a wide range of scales (e.g., recycled materials, primordial heterogeneity), and this macro-scale heterogeneity should be accounted for during the inversion of geophysical data.

FUTURE ISSUES

1. A better understanding of (*a*) the bulk composition of Earth relative to the chondritic paradigm for major elements, particularly Fe, Mg, and Si, and (*b*) the Si content of the core is needed to break the degeneracy between plausible compositional models of the lower mantle.
2. Additional high *P-T* experiments with varying iron content are required for improved understanding of the effects of the Fe-spin transition on the elasticity of bridgmanite and ferropericlase.
3. There is further need of evaluation of the effect of the coupled incorporation of Fe^{3+} and Al_2O_3 on bridgmanite elasticity.
4. A more definitive approach to comparing mineral physics measurements with geophysical data/models would be to merge the experimental data with the thermodynamic database for the relevant end members and to re-perform the geophysical inversion following the approach laid out here. This would ensure that the derived models of interior structure are based on (*a*) geophysical data, including full consideration of data uncertainties; (*b*) quantitative comparison with data; (*c*) a variable compositional

and mineralogical model, including the most up-to-date thermoelastic parameters; (*d*) self-consistent model computations; and, finally, (*e*) encapsulating uncertainties in thermodynamic parameters either a posteriori via a hybrid strategy or directly in the inversion.

5. To better understand the dynamics of mixing and preservation of silica-enriched heterogeneity in the (lower) mantle, numerical models with more realistic rheology (e.g., grain-size and fabric dependent) and distribution of heat-producing elements are needed.
6. Future geodynamic models should also aim to treat the transition from magma-ocean crystallization to solid-state convection and long-term mantle evolution self-consistently.

DISCLOSURE STATEMENT

The authors are not aware of any affiliations, memberships, funding, or financial holdings that might be perceived as affecting the objectivity of this review.

ACKNOWLEDGMENTS

The authors are grateful to Federico D. Munch for help with **Figures 3** and **5**. They also thank Anna Gülcher for the raw version of **Figure 6**. We also thank Roberta Rudnick for comments on the paper. P.A.S. thanks the Swiss National Science Foundation via an Eccellenza Professorship (203668) and the Swiss State Secretariat for Education, Research and Innovation (SERI) under contract MB22.00033, a SERI-funded ERC Starting Grant 2ATMO. M.M. thanks the ETH Startup fund. M.D.B. acknowledges NERC grant NE/X000508/1.

LITERATURE CITED

Abers GA, Hacker BR. 2016. A MATLAB toolbox and Excel workbook for calculating the densities, seismic wave speeds, and major element composition of minerals and rocks at pressure and temperature. *Geochem. Geophys. Geosyst.* 17(2):616–24

Afonso JC, Fullea J, Griffin WL, Yang Y, Jones AG, et al. 2013. 3-D multiobservable probabilistic inversion for the compositional and thermal structure of the lithosphere and upper mantle. I: A priori petrological information and geophysical observables. *J. Geophys. Res. Solid Earth* 118(5):2586–617

Allègre CJ, Poirier JP, Humler E, Hofmann AW. 1995. The chemical composition of the Earth. *Earth Planet. Sci. Lett.* 134(3):515–26

Anderson OL. 1982. The Earth's core and the phase-diagram of iron. *Philos. Trans. R. Soc. A* 306:21–35

Anzellini S, Dewaele A, Mezouar M, Loubeyre P, Morard G. 2013. Melting of iron at Earth's inner core boundary based on fast X-ray diffraction. *Science* 340(6131):464–66

Badro J. 2014. Spin transitions in mantle minerals. *Annu. Rev. Earth Planet. Sci.* 42:231–48

Badro J, Côté AS, Brodholt JP. 2014. A seismologically consistent compositional model of Earth's core. *PNAS* 111(21):7542–45

Baker MB, Beckett JR. 1999. The origin of abyssal peridotites: a reinterpretation of constraints based on primary bulk compositions. *Earth Planet. Sci. Lett.* 171(1):49–61

Baker MB, Stolper EM. 1994. Determining the composition of high-pressure mantle melts using diamond aggregates. *Geochim. Cosmochim. Acta* 58(13):2811–27

Ballmer MD, Houser C, Hernlund JW, Wentzcovitch RM, Hirose K. 2017a. Persistence of strong silica-enriched domains in the Earth's lower mantle. *Nat. Geosci.* 10(3):236–40

Ballmer MD, Lourenço DL, Hirose K, Caracas R, Nomura R. 2017b. Reconciling magma-ocean crystallization models with the present-day structure of the Earth's mantle. *Geochem. Geophys. Geosyst.* 18(7):2785–806

Ballmer MD, Schmerr NC, Nakagawa T, Ritsema J. 2015. Compositional mantle layering revealed by slab stagnation at ~1000-km depth. *Sci. Adv.* 1(11):e1500815

Bina CR. 1998. Free energy minimization by simulated annealing with applications to lithospheric slabs and mantle plumes. *Pure Appl. Geophys.* 151(2–4):605–18

Bina CR, Helffrich G. 2014. Geophysical constraints on mantle composition. In *Treatise on Geochemistry*, ed. HD Holland, KK Turekian, pp. 41–65. Oxford, UK: Elsevier. 2nd ed.

Bissig F, Khan A, Giardini D. 2022a. Evidence for basalt enrichment in the mantle transition zone from inversion of triplicated P- and S-waveforms. *Earth Planet. Sci. Lett.* 580:117387

Bissig F, Khan A, Giardini D. 2022b. Joint inversion of PP and SS precursor waveforms and Rayleigh wave phase velocities for global mantle transition zone structure. *Geophys. J. Int.* 233:316–37

Boukaré CE, Ricard Y, Fiquet G. 2015. Thermodynamics of the MgO-FeO-SiO_2 system up to 140 GPa: application to the crystallization of Earth's magma ocean. *J. Geophys. Res. Solid Earth* 120(9):6085–101

Boyd F. 1989. Compositional distinction between oceanic and cratonic lithosphere. *Earth Planet. Sci. Lett.* 96(1–2):15–26

Brandenburg J, Van Keken P. 2007. Deep storage of oceanic crust in a vigorously convecting mantle. *J. Geophys. Res.* 112(B6):B06403

Cabral RA, Jackson MG, Rose-Koga EF, Koga KT, Whitehouse MJ, et al. 2013. Anomalous sulphur isotopes in plume lavas reveal deep mantle storage of Archaean crust. *Nature* 496(7446):490–93

Cammarano F, Goes S, Deuss A, Giardini D. 2005. Is a pyrolitic adiabatic mantle compatible with seismic data? *Earth Planet. Sci. Lett.* 232(3–4):227–43

Canil D. 2004. Mildly incompatible elements in peridotites and the origins of mantle lithosphere. *Lithos* 77(1–4):375–93

Caracas R, Hirose K, Nomura R, Ballmer MD. 2019. Melt–crystal density crossover in a deep magma ocean. *Earth Planet. Sci. Lett.* 516:202–11

Chust TC, Steinle-Neumann G, Dolejš D, Schuberth BSA, Bunge HP. 2017. MMA-EoS: a computational framework for mineralogical thermodynamics. *J. Geophys. Res. Solid Earth* 122(12):9881–920

Cobden L, Goes S, Ravenna M, Styles E, Cammarano F, et al. 2009. Thermochemical interpretation of 1-D seismic data for the lower mantle: the significance of nonadiabatic thermal gradients and compositional heterogeneity. *J. Geophys. Res.* 114(B11):B11309

Connolly JAD. 2009. The geodynamic equation of state: what and how. *Geochem. Geophys. Geosyst.* 10(10):Q10014

Connolly JAD, Kerrick DM. 2002. Metamorphic controls on seismic velocity of subducted oceanic crust at 100–250 km depth. *Earth Planet. Sci. Lett.* 204(1–2):61–74

Connolly JAD, Khan A. 2016. Uncertainty of mantle geophysical properties computed from phase equilibrium models. *Geophys. Res. Lett.* 43:5026–34

Corgne A, Liebske C, Wood BJ, Rubie DC, Frost DJ. 2005. Silicate perovskite-melt partitioning of trace elements and geochemical signature of a deep perovskitic reservoir. *Geochim. Cosmochim. Acta* 69(2):485–96

Costa A, Caricchi L, Bagdassarov N. 2009. A model for the rheology of particle-bearing suspensions and partially molten rocks. *Geochem. Geophys. Geosyst.* 10(3):Q03010

Criniti G, Kurnosov A, Boffa Ballaran T, Frost DJ. 2021. Single-crystal elasticity of $MgSiO_3$ bridgmanite to mid-lower mantle pressure. *J. Geophys. Res. Solid Earth* 126:e2020JB020967

da Silva CRS, Wentzcovitch RM, Patel A, Price GD, Karato SI. 2000. The composition and geotherm of the lower mantle: constraints from the elasticity of silicate perovskite. *Phys. Earth Planet. Inter.* 118(1–2):103–9

Dauphas N, Poitrasson F, Burkhardt C, Kobayashi H, Kurosawa K. 2015. Planetary and meteoritic Mg/Si and δ30Si variations inherited from solar nebula chemistry. *Earth Planet. Sci. Lett.* 427:236–48

Davaille A. 1999. Simultaneous generation of hotspots and superswells by convection in a heterogeneous planetary mantle. *Nature* 402(6763):756–60

Deng H, Ballmer MD, Reinhardt C, Meier MM, Mayer L, et al. 2019. Primordial Earth mantle heterogeneity caused by the Moon-forming giant impact? *Astrophys. J.* 887(2):211
Dorfman SM, Duffy TS. 2014. Effect of Fe-enrichment on seismic properties of perovskite and post-perovskite in the deep lower mantle. *Geophys. J. Int.* 197:910–19
Dziewonski AM, Anderson DL. 1981. Preliminary reference Earth model. *Phys. Earth Planet. Inter.* 25:297–356
Fabrichnaya O, Saxena K, Richet P, Westrum EF, eds. 2004. *Thermodynamic Data, Models, and Phase Diagrams in Multicomponent Oxide Systems*. Heidelberg, Ger.: Springer
Fei H, Ballmer MD, Faul U, Walte N, Cao W, Katsura T. 2023. Variation in bridgmanite grain size accounts for the mid-mantle viscosity jump. *Nature* 620(7975):794–99
Fei Y, Zhang L, Corgne A, Watson H, Ricolleau A, et al. 2007. Spin transition and equations of state of (Mg,Fe)O solid solutions. *Geophys. Res. Lett.* 34:L17307
Ferrachat S, Ricard Y. 1998. Regular versus chaotic mantle mixing. *Earth Planet. Sci. Lett.* 155(1–2):75–86
Fitoussi C, Bourdon B, Kleine T, Oberli F, Reynolds BC. 2009. Si isotope systematics of meteorites and terrestrial peridotites: implications for Mg/Si fractionation in the solar nebula and for Si in the Earth's core. *Earth Planet. Sci. Lett.* 287(1–2):77–85
French SW, Romanowicz B. 2015. Broad plumes rooted at the base of the Earth's mantle beneath major hotspots. *Nature* 525(7567):95–99
Frossard P, Israel C, Bouvier A, Boyet M. 2022. Earth's composition was modified by collisional erosion. *Science* 377(6614):1529–32
Frost DJ, Myhill R. 2016. Chemistry of the lower mantle. In *Deep Earth: Physics and Chemistry of the Lower Mantle Core*, ed. H Terasaki, RA Fischer, pp. 225–40. Hoboken, NJ: Wiley
Fu S, Zhang Y, Okuchi T, Lin JF. 2023. Single-crystal elasticity of (Al,Fe)-bearing bridgmanite up to 82 GPa. *Am. Miner.* 108:719–30
Fukao Y, Obayashi M. 2013. Subducted slabs stagnant above, penetrating through, and trapped below the 660 km discontinuity. *J. Geophys. Res. Solid Earth* 118(11):5920–38
Fullea J, Lebedev S, Martinec Z, Celli NL. 2021. WINTERC-G: mapping the upper mantle thermochemical heterogeneity from coupled geophysical–petrological inversion of seismic waveforms, heat flow, surface elevation and gravity satellite data. *Geophys. J. Int.* 226:146–91
Ganguly J, Freed AM, Saxena SK. 2009. Density profiles of oceanic slabs and surrounding mantle: integrated thermodynamic and thermal modeling, and implications for the fate of slabs at the 660 km discontinuity. *Phys. Earth Planet. Inter.* 172(3–4):257–67
Girard J, Amulele G, Farla R, Mohiuddin A, Karato S. 2016. Shear deformation of bridgmanite and magnesiowüstite aggregates at lower mantle conditions. *Science* 351(6269):144–47
Goes S, Yu C, Ballmer MD, Yan J, van der Hilst RD. 2022. Compositional heterogeneity in the mantle transition zone. *Nat. Rev. Earth Environ.* 3(8):533–50
Grayver AV, Munch FD, Kuvshinov AV, Khan A, Sabaka TJ, Tøffner-Clausen L. 2017. Joint inversion of satellite-detected tidal and magnetospheric signals constrains electrical conductivity and water content of the upper mantle and transition zone. *Geophys. Res. Lett.* 44(12):6074–81
Gülcher AJP, Ballmer MD, Tackley PJ. 2021. Coupled dynamics and evolution of primordial and recycled heterogeneity in Earth's lower mantle. *Solid Earth* 12(9):2087–107
Gülcher AJP, Gebhardt DJ, Ballmer MD, Tackley PJ. 2020. Variable dynamic styles of primordial heterogeneity preservation in the Earth's lower mantle. *Earth Planet. Sci. Lett.* 536:116160
Hacker BR, Abers GA. 2004. Subduction Factory 3: an Excel worksheet and macro for calculating the densities, seismic wave speeds, and H_2O contents of minerals and rocks at pressure and temperature. *Geochem. Geophys. Geosyst.* 5(1):Q01005
Hart SR, Zindler A. 1986. In search of a bulk Earth composition. *Chem. Geol.* 57:247–67
Helffrich G, Ballmer MD, Hirose K. 2018. Core-exsolved SiO_2 dispersal in the Earth's mantle. *J. Geophys. Res. Solid Earth* 123(1):176–88
Herzberg C. 2004. Geodynamic information in peridotite petrology. *J. Petrol.* 45(12):2507–30
Herzberg C, Asimow P. 2015. PRIMELT 3 MEGA. XLSM software for primary magma calculation: peridotite primary magma MgO contents from the liquidus to the solidus. *Geochem. Geophys. Geosyst.* 16(2):563–78
Herzberg C, Condie K, Korenaga J. 2010. Thermal history of the Earth and its petrological expression. *Earth Planet. Sci. Lett.* 292(1–2):79–88

Hier-Majumder S, Hirschmann MM. 2017. The origin of volatiles in the Earth's mantle. *Geochem. Geophys. Geosyst.* 18(8):3078–92

Hirose K, Morard G, Sinmyo R, Umemoto K, Hernlund J, et al. 2017. Crystallization of silicon dioxide and compositional evolution of the Earth's core. *Nature* 543(7643):99–102

Hirose K, Wood B, Vočadlo L. 2021. Light elements in the Earth's core. *Nat. Rev. Earth Environ.* 2(9):645–58

Holtzman B, Groebner N, Zimmerman M, Ginsberg S, Kohlstedt D. 2003. Stress-driven melt segregation in partially molten rocks. *Geochem. Geophys. Geosyst.* 4(5):8607

Huang D, Badro J, Brodholt J, Li Y. 2019. Ab initio molecular dynamics investigation of molten Fe–Si–O in Earth's core. *Geophys. Res. Lett.* 46(12):6397–405

Huang R, Ballaran TB, McCammon CA, Miyajima N, Dolejš D, Frost DJ. 2021. The composition and redox state of bridgmanite in the lower mantle as a function of oxygen fugacity. *Geochim. Cosmochim. Acta* 303:110–36

Irifune T. 1994. Phase transformations in pyrolite and subducted crust compositions down to a depth of 800 km in the lower mantle. *Mineral. Mag.* 58A(1):444–45

Irifune T, Shinmei T, McCammon C, Miyajima N, Rubie D, Frost D. 2010. Iron partitioning and density changes of pyrolite in Earth's lower mantle. *Science* 327:193–95

Irving JCE, Cottaar S, Lekic V. 2018. Seismically determined elastic parameters for Earth's outer core. *Sci. Adv.* 4(6):eaar2538

Ita J, Stixrude L. 1992. Petrology, elasticity, and composition of the mantle transition zone. *J. Geophys. Res. Atmos.* 97(B5):6849–66

Jackson CR, Ziegler LB, Zhang H, Jackson MG, Stegman DR. 2014. A geochemical evaluation of potential magma ocean dynamics using a parameterized model for perovskite crystallization. *Earth Planet. Sci. Lett.* 392:154–65

Jackson I. 1998. Elasticity, composition and temperature of the Earth's lower mantle: a reappraisal. *Geophys. J. Int.* 134(1):291–311

Jackson I, Rigden SM. 1998. Composition and temperature of the Earth's mantle: seismological models interpreted through experimental studies of Earth materials. In *The Earth's Mantle: Composition, Structure and Evolution*, ed. I Jackson, pp. 405–60. Cambridge, UK: Cambridge Univ. Press

Jackson JM, Zhang J, Shu J, Sinogeikin SV, Bass JD. 2005. High-pressure sound velocities and elasticity of aluminous $MgSiO_3$ perovskite to 45 GPa: implications for lateral heterogeneity in Earth's lower mantle. *Geophys. Res. Lett.* 32:L21305

Jacobsen SD, Reichmann HJ, Spetzler HA, Mackwell SJ, Smyth JR, et al. 2002. Structure and elasticity of single-crystal (Mg,Fe)O and a new method of generating shear waves for gigahertz ultrasonic interferometry. *J. Geophys. Res.* 107(B2):ECV-4

Jagoutz E, Palme H, Baddenhausen H, Blum K, Cendales M, et al. 1979. The abundances of major, minor and trace elements in the Earth's mantle as derived from primitive ultramafic nodules. In *Proceedings of the Tenth Lunar and Planetary Science Conference, Houston, Texas, March 19–23, 1979*, ed. RB Merrill, pp. 2031–50. New York: Pergamon

Jenkins J, Deuss A, Cottaar S. 2017. Converted phases from sharp 1000 km depth mid-mantle heterogeneity beneath Western Europe. *Earth Planet. Sci. Lett.* 459:196–207

Jenner FE, O'Neill HSC. 2012. Analysis of 60 elements in 616 ocean floor basaltic glasses. *Geochem. Geophys. Geosyst.* 13(2):Q02005

Kaneshima S, Helffrich G. 2010. Small scale heterogeneity in the mid-lower mantle beneath the circum-Pacific area. *Phys. Earth Planet. Inter.* 183(1–2):91–103

Katsura T. 2022. A revised adiabatic temperature profile for the mantle. *J. Geophys. Res. Solid Earth* 127(2):e2021JB023562

Kellogg LH, Hager BH, van der Hilst RD. 1999. Compositional stratification in the deep mantle. *Science* 283(5409):1881–84

Kemper J. 2023. *Modern computational methods applied to classical long-period seismology*. PhD Thesis, ETH Zürich, Zürich, Switz.

Kennett BLN, Jackson I. 2009. Optimal equations of state for mantle minerals from simultaneous non-linear inversion of multiple datasets. *Phys. Earth Planet. Inter.* 176(1–2):98–108

Khan A. 2016. On Earth's mantle constitution and structure from joint analysis of geophysical and laboratory-based data: an example. *Surv. Geophys.* 37:149–89

Khan A, Boschi L, Connolly JAD. 2009. On mantle chemical and thermal heterogeneities and anisotropy as mapped by inversion of global surface wave data. *J. Geophys. Res.* 114(B9):B09305

Khan A, Connolly JAD, Olsen N. 2006. Constraining the composition and thermal state of the mantle beneath Europe from inversion of long-period electromagnetic sounding data. *J. Geophys. Res.* 111(B10):B10102

Khan A, Connolly JAD, Taylor SR. 2008. Inversion of seismic and geodetic data for the major element chemistry and temperature of the Earth's mantle. *J. Geophys. Res.* 113(B9):B09308

Khan A, Sossi PA, Liebske C, Rivoldini A, Giardini D. 2022. Geophysical and cosmochemical evidence for a volatile-rich Mars. *Earth Planet. Sci. Lett.* 578:117330

Korenaga J. 2013. Initiation and evolution of plate tectonics on Earth: theories and observations. *Annu. Rev. Earth Planet. Sci.* 41:117–51

Koyama T, Khan A, Kuvshinov A. 2014. Three-dimensional electrical conductivity structure beneath Australia from inversion of geomagnetic observatory data: evidence for lateral variations in transition-zone temperature, water content and melt. *Geophys. J. Int.* 196(3):1330–50

Kung J, Li B, Weidner DJ, Zhang J, Liebermann RC. 2002. Elasticity of $(Mg_{0.83},Fe_{0.17})O$ ferropericlase at high pressure: ultrasonic measurements in conjunction with X-radiation techniques. *Earth Planet. Sci. Lett.* 203(1):557–66

Kurnosov A, Marquardt H, Frost DJ, Ballaran TB, Ziberna L. 2017. Evidence for a Fe^{3+}-rich pyrolitic lower mantle from (Al,Fe)-bearing bridgmanite elasticity data. *Nature* 543:543–46

Kuskov OL, Fabrichnaya OB. 1994. Constitution of the Moon: 2. Composition and seismic properties of the lower mantle. *Phys. Earth Planet. Inter.* 83(3–4):197–216

Labrosse S, Hernlund J, Coltice N. 2007. A crystallizing dense magma ocean at the base of the Earth's mantle. *Nature* 450(7171):866–69

Larimer JW. 1967. Chemical fractionations in meteorites—i. Condensation of the elements. *Geochim. Cosmochim. Acta* 31(8):1215–38

Lau HC, Mitrovica JX, Austermann J, Crawford O, Al-Attar D, Latychev K. 2016. Inferences of mantle viscosity based on ice age data sets: radial structure. *J. Geophys. Res. Solid Earth* 121(10):6991–7012

Lau HC, Mitrovica JX, Davis JL, Tromp J, Yang HY, Al-Attar D. 2017. Tidal tomography constrains Earth's deep-mantle buoyancy. *Nature* 551(7680):321–26

Lebrun T, Massol H, Chassefière E, Davaille A, Marcq E, et al. 2013. Thermal evolution of an early magma ocean in interaction with the atmosphere. *J. Geophys. Res. Planets* 118(6):1155–76

Liebske C, Corgne A, Frost DJ, Rubie DC, Wood BJ. 2005. Compositional effects on element partitioning between Mg-silicate perovskite and silicate melts. *Contrib. Mineral. Petrol.* 149:113–28

Lin JF, Mao Z, Yang J, Fu S. 2018. Elasticity of lower-mantle bridgmanite. *Nature* 564:E18–26

Lodders K. 2003. Solar system abundances and condensation temperatures of the elements. *Astrophys. J.* 591(2):1220

Lourenço DL, Rozel AB, Ballmer MD, Tackley PJ. 2020. Plutonic-squishy lid: a new global tectonic regime generated by intrusive magmatism on Earth-like planets. *Geochem. Geophys. Geosyst.* 21(4):e2019GC008756

Lundin S, Catalli K, Santillàn J, Shim SH, Prakapenka VB, et al. 2008. Effect of Fe on the equation of state of mantle silicate perovskite over 1 Mbar. *Phys. Earth Planet. Inter.* 168:97–102

Lyubetskaya T, Korenaga J. 2007. Chemical composition of Earth's primitive mantle and its variance: 1. Method and results. *J. Geophys. Res.* 112(B3):B03211

Manga M. 1996. Mixing of heterogeneities in the mantle: effect of viscosity differences *Geophys. Res. Lett.* 23(4):403–6

Marquardt H, Speziale S, Reichmann HJ, Frost DJ, Schilling FR, Garnero EJ. 2009. Elastic shear anisotropy of ferropericlase in Earth's lower mantle. *Science* 324(5924):224–26

Marton FC, Cohen RE. 2002. Constraints on lower mantle composition from molecular dynamics simulations of $MgSiO_3$ perovskite. *Phys. Earth Planet. Inter.* 134:239–52

Mashino I, Murakami M, Miyajima N, Petitgirard S. 2020. Experimental evidence for silica-enriched Earth's lower mantle with ferrous iron dominant bridgmanite. *PNAS* 117:27899–905

Matas J, Bass J, Ricard Y, Mattern E, Bukowinski MST. 2007. On the bulk composition of the lower mantle: predictions and limitations from generalized inversion of radial seismic profiles. *Geophys. J. Int.* 170(2):764–80

Mattern E, Matas J, Ricard Y, Bass J. 2005. Lower mantle composition and temperature from mineral physics and thermodynamic modelling. *Geophys. J. Int.* 160(3):973–90

Matthews KJ, Maloney KT, Zahirovic S, Williams SE, Seton M, Müller RD. 2016. Global plate boundary evolution and kinematics since the late Paleozoic. *Glob. Planet. Change* 146:226–50

McDonough WF, Sun SS. 1995. The composition of the Earth. *Chem. Geol.* 120(3–4):223–53

Miyazaki Y, Korenaga J. 2019. On the timescale of magma ocean solidification and its chemical consequences: 1. Thermodynamic database for liquid at high pressures. *J. Geophys. Res. Solid Earth* 124(4):3382–98

Moore WB, Webb AAG. 2013. Heat-pipe Earth. *Nature* 501(7468):501–5

Morgan JP, Morgan WJ. 1999. Two-stage melting and the geochemical evolution of the mantle: a recipe for mantle plum-pudding. *Earth Planet. Sci. Lett.* 170(3):215–39

Munch FD, Khan A, Tauzin B, van Driel M, Giardini D. 2020. Seismological evidence for thermo-chemical heterogeneity in Earth's continental mantle. *Earth Planet. Sci. Lett.* 539:116240

Murakami M. 2013. Chemical composition of the Earth's lower mantle: constraints from elasticity. *Phys. Chem. Deep Earth* 3:183–212

Murakami M, Asahara Y, Ohishi Y, Hirao N, Hirose K. 2009. Development of in situ Brillouin spectroscopy at high pressure and high temperature with synchrotron radiation and infrared laser heating system: application to the Earth's deep interior. *Phys. Earth Planet. Inter.* 174:282–91

Murakami M, Hirose K, Sata N, Ohishi Y. 2005. Post-perovskite phase transition and mineral chemistry in the pyrolitic lowermost mantle. *Geophys. Res. Lett.* 32:L03304

Murakami M, Ohishi Y, Hirao N, Hirose K. 2012. A perovskitic lower mantle inferred from high-pressure, high-temperature sound velocity data. *Nature* 485:90–94

Murakami M, Sinogeikin SV, Bass JD, Sata N, Ohishi Y, Hirose K. 2007b. Sound velocity of $MgSiO_3$ post-perovskite phase: a constraint on the *D″* discontinuity. *Earth Planet. Sci. Lett.* 259:18–23

Murakami M, Sinogeikin SV, Hellwig H, Bass JD, Li J. 2007a. Sound velocity of $MgSiO_3$ perovskite to Mbar pressure. *Earth Planet. Sci. Lett.* 256:47–54

Myhill R, Cottaar S, Heister T, Rose I, Unterborn C, et al. 2023. BurnMan—a Python toolkit for planetary geophysics, geochemistry and thermodynamics. *J. Open Source Softw.* 8(87):5389

Nabiei F, Badro J, Boukaré CÉ, Hébert C, Cantoni M, et al. 2021. Investigating magma ocean solidification on Earth through laser-heated diamond anvil cell experiments. *Geophys. Res. Lett.* 48(12):e2021GL092446

Nakagawa T, Buffett BA. 2005. Mass transport mechanism between the upper and lower mantle in numerical simulations of thermochemical mantle convection with multicomponent phase changes. *Earth Planet. Sci. Lett.* 230(1–2):11–27

Nakajima M, Stevenson DJ. 2015. Melting and mixing states of the Earth's mantle after the Moon-forming impact. *Earth Planet. Sci. Lett.* 427:286–95

Nisbet E, Cheadle M, Arndt N, Bickle M. 1993. Constraining the potential temperature of the Archaean mantle: a review of the evidence from komatiites. *Lithos* 30(3–4):291–307

Nomura R, Hirose K, Uesugi K, Ohishi Y, Tsuchiyama A, et al. 2014. Low core-mantle boundary temperature inferred from the solidus of pyrolite. *Science* 343(6170):522–25

O'Neill CJ, Zhang S. 2018. Lateral mixing processes in the Hadean. *J. Geophys. Res. Solid Earth* 123(8):7074–89

O'Neill HSC, Canil D, Rubie DC. 1998. Oxide-metal equilibria to 2500°C and 25 GPa: implications for core formation and the light component in the Earth's core. *J. Geophys. Res.* 103(B6):12239–60

O'Neill HSC, Palme H. 1998. Composition of the silicate Earth: implications for accretion and core formation. In *The Earth's Mantle*, ed. I Jackson, pp. 3–126. Cambridge, UK: Cambridge Univ. Press

O'Neill HSC, Palme H. 2008. Collisional erosion and the non-chondritic composition of the terrestrial planets. *Philos. Trans. R. Soc. A* 366(1883):4205–38

Palme H, O'Neill HSC. 2014. Cosmochemical estimates of mantle composition. In *Treatise on Geochemistry*, ed. HD Holland, KK Turekian, pp. 1–36. Oxford, UK: Elsevier. 2nd ed.

Piazzoni AS, Steinle-Neumann G, Bunge HP, Dolejš D. 2007. A mineralogical model for density and elasticity of the Earth's mantle. *Geochem. Geophys. Geosyst.* 8(11):Q11010

Piet H, Badro J, Nabiei F, Dennenwaldt T, Shim SH, et al. 2016. Spin and valence dependence of iron partitioning in Earth's deep mantle. *PNAS* 113(40):11127–30
Poirier JP. 1994. Light elements in the Earth's outer core: a critical review. *Phys. Earth Planet. Inter.* 85(3–4):319–37
Puchtel IS, Blichert-Toft J, Horan MF, Touboul M, Walker RJ. 2022. The komatiite testimony to ancient mantle heterogeneity. *Chem. Geol.* 594:120776
Ricard Y, Mattern E, Matas J. 2005. Synthetic tomographic images of slabs from mineral physics. In *Changing Views on the Structure, Composition, and Evolution of Earth's Deep*, ed. RD van der Hilst, JD Bass, J Matas, J Trampert, pp. 283–300. Washington, DC: Am. Geophys. Union
Ricolleau A, Fei Y, Corgne A, Siebert J, Badro J. 2011. Oxygen and silicon contents of Earth's core from high pressure metal–silicate partitioning experiments. *Earth Planet. Sci. Lett.* 310(3–4):409–21
Ringwood AE. 1966. Chemical evolution of the terrestrial planets. *Geochim. Cosmochim. Acta* 30(1):41–104
Ringwood AE. 1975. *Composition and Petrology of the Earth's Mantle*. New York: McGraw-Hill
Ringwood AE. 1979. *Origin of the Earth and Moon*. New York: Springer
Rudolph ML, Lekić V, Lithgow-Bertelloni C. 2015. Viscosity jump in Earth's mid-mantle. *Science* 350(6266):1349–52
Schuberth BSA, Bunge HP, Ritsema J. 2009. Tomographic filtering of high-resolution mantle circulation models: Can seismic heterogeneity be explained by temperature alone? *Geochem. Geophys. Geosyst.* 10(5):Q05W03
Shephard GE, Houser C, Hernlund JW, Valencia-Cardona JJ, Trønnes RG, Wentzcovitch RM. 2021. Seismological expression of the iron spin crossover in ferropericlase in the Earth's lower mantle. *Nat. Commun.* 12(1):5905
Sinmyo R, Hirose K, Nishio-Hamane D, Seto Y, Fujino K, et al. 2008. Partitioning of iron between perovskite/postperovskite and ferropericlase in the lower mantle. *J. Geophys. Res.* 113(B11):B11204
Sinogeikin SV, Bass JD. 2000. Single-crystal elasticity of pyrope and MgO to 20 GPa by Brillouin scattering in the diamond cell. *Phys. Earth Planet. Inter.* 120:43–62
Sizova E, Gerya T, Brown M, Perchuk L. 2010. Subduction styles in the Precambrian: insight from numerical experiments. *Lithos* 116(3–4):209–29
Solomatov V. 2015. Magma oceans and primordial mantle differentiation. In *Treatise on Geophysics*, ed. G Schubert, pp. 91–119. Amsterdam: Elsevier
Sossi PA, Eggins SM, Nesbitt RW, Nebel O, Hergt JM, et al. 2016. Petrogenesis and geochemistry of Archean komatiites. *J. Petrol.* 57(1):147–84
Sossi PA, Nebel O, O'Neill HSC, Moynier F. 2018. Zinc isotope composition of the Earth and its behaviour during planetary accretion. *Chem. Geol.* 477:73–84
Spray JG. 1989. Upper mantle segregation processes: evidence from alpine-type peridotites. *Geol. Soc. Lond. Spec. Publ.* 42(1):29–40
Stixrude L, Lithgow-Bertelloni C. 2005. Thermodynamics of mantle minerals—I. Physical properties. *Geophys. J. Int.* 162(2):610–32
Stixrude L, Lithgow-Bertelloni C. 2011. Thermodynamics of mantle minerals—II. Phase equilibria. *Geophys. J. Int.* 184(3):1180–213
Stixrude L, Lithgow-Bertelloni C. 2021. Thermal expansivity, heat capacity and bulk modulus of the mantle. *Geophys. J. Int.* 228(2):1119–49
Tackley PJ, Xie S, Nakagawa T, Hernlund JW. 2005. Numerical and laboratory studies of mantle convection: philosophy, accomplishments, and thermochemical structure and evolution. *Geophys. Monogr.* 160(83):2190
Tauzin B, Waszek L, Ballmer MD, Afonso JC, Bodin T. 2022. Basaltic reservoirs in the Earth's mantle transition zone. *PNAS* 119(48):e2209399119
Tolstikhin I, Hofmann AW. 2005. Early crust on top of the Earth's core. *Phys. Earth Planet. Inter.* 148(2–4):109–30
Trampert J, Deschamps F, Resovsky J, Yuen D. 2004. Probabilistic tomography maps chemical heterogeneities throughout the lower mantle. *Science* 306(5697):853–56
Tsujino N, Yamazaki D, Nishihara Y, Yoshino T, Higo Y, Tange Y. 2022. Viscosity of bridgmanite determined by in situ stress and strain measurements in uniaxial deformation experiments. *Sci. Adv.* 8(13):eabm1821

Umemoto K, Hirose K. 2020. Chemical compositions of the outer core examined by first principles calculations. *Earth Planet. Sci. Lett.* 531:116009

Van Der Meer DG, Spakman W, Van Hinsbergen DJ, Amaru ML, Torsvik TH. 2010. Towards absolute plate motions constrained by lower-mantle slab remnants. *Nat. Geosci.* 3(1):36–40

Vilella K, Bodin T, Boukaré CE, Deschamps F, Badro J, et al. 2021. Constraints on the composition and temperature of LLSVPs from seismic properties of lower mantle minerals. *Earth Planet. Sci. Lett.* 554:116685

Walter MJ. 1998. Melting of garnet peridotite and the origin of komatiite and depleted lithosphere. *J. Petrol.* 39(1):29–60

Walter MJ. 2003. Melt extraction and compositional variability in mantle lithosphere. In *Treatise on Geochemistry*, ed. HD Holland, KK Turekian, pp. 363–94. Oxford, UK: Pergamon

Walter MJ, Nakamura E, Trønnes R, Frost D. 2004. Experimental constraints on crystallization differentiation in a deep magma ocean. *Geochim. Cosmochim. Acta* 68(20):4267–84

Wasson JT, Kallemeyn GW. 1988. Compositions of chondrites. *Philos. Trans. R. Soc. A* 325(1587):535–44

Waszek L, Schmerr NC, Ballmer MD. 2018. Global observations of reflectors in the mid-mantle with implications for mantle structure and dynamics. *Nat. Commun.* 9(1):385

Waszek L, Tauzin B, Schmerr NC, Ballmer MD, Afonso JC. 2021. A poorly mixed mantle transition zone and its thermal state inferred from seismic waves. *Nat. Geosci.* 14(12):949–55

Weidner DJ. 1985. A mineral physics test of a pyrolite mantle. *Geophys. Res. Lett.* 12(7):417–20

Weidner DJ, Swyler K, Carleton HR. 1975. Elasticity of microcrystals. *Geophys. Res. Lett.* 2:189–92

Wilson AH. 2019. The late-Paleoarchean ultra-depleted Commondale komatiites: Earth's hottest lavas and consequences for eruption. *J. Petrol.* 60(8):1575–620

Witt-Eickschen G, Palme H, O'Neill HSC, Allen CM. 2009. The geochemistry of the volatile trace elements As, Cd, Ga, In and Sn in the Earth's mantle: new evidence from in situ analyses of mantle xenoliths. *Geochim. Cosmochim. Acta* 73(6):1755–78

Workman RK, Hart SR. 2005. Major and trace element composition of the depleted MORB mantle (DMM). *Earth Planet. Sci. Lett.* 231(1–2):53–72

Xie L, Yoneda A, Yamazaki D, Manthilake G, Higo Y, et al. 2020. Formation of bridgmanite-enriched layer at the top lower-mantle during magma ocean solidification. *Nat. Commun.* 11(1):548

Xu F, Yamazaki D, Sakamoto N, Sun W, Fei H, Yurimoto H. 2017. Silicon and oxygen self-diffusion in stishovite: implications for stability of SiO_2-rich seismic reflectors in the mid-mantle. *Earth Planet. Sci. Lett.* 459:332–39

Xu W, Lithgow-Bertelloni C, Stixrude L, Ritsema J. 2008. The effect of bulk composition and temperature on mantle seismic structure. *Earth Planet. Sci. Lett.* 275(1–2):70–79

Xu Y, Shankland TJ, Poe BT. 2000. Laboratory-based electrical conductivity in the Earth's mantle. *J. Geophys. Res.* 105(B12):27865–75

Yan J, Ballmer MD, Tackley PJ. 2020. The evolution and distribution of recycled oceanic crust in the Earth's mantle: insight from geodynamic models. *Earth Planet. Sci. Lett.* 537:116171

Yang R, Wu Z. 2014. Elastic properties of stishovite and the $CaCl_2$-type silica at the mantle temperature and pressure: an ab initio investigation. *Earth Planet. Sci. Lett.* 404:14–21

Yoneda S, Grossman L. 1995. Condensation of $CaO–MgO–Al_2O_3–SiO_2$ liquids from cosmic gases. *Geochim. Cosmochim. Acta* 59(16):3413–44

Yoshizaki T, McDonough WF. 2021. Earth and Mars—distinct inner solar system products. *Geochemistry* 81(2):125746

Zunino A, Connolly JAD, Khan A. 2011. Pre-calculated phase equilibrium models for geophysical properties of the crust and mantle as a function of composition. *Geochem. Geophys. Geosyst.* 12:Q04001